UiT The Arctic University of Norway

Faculty of Science and Technology
Department of Physics and Technology

The effect of a water-ice mantle on dust trajectories in the Kuiper belt

Amalie Gjelsvik

FYS-3931 Master's thesis in Space Physics 30 SP
July 2023

Abstract

The New Horizons spacecraft has travelled through the Solar System and has reached a distance of 55 AU as of 2023. For one of the first times, the dust flux in the outer Solar System has been measured, using the instrument Student Dust Counter (SDC) onboard New Horizons. Between 30 and 50 AU is the Kuiper belt, which is a disk consisting of icy objects. These objects can undergo collisions, causing them to fragment and generate smaller objects, such as dust grains. The SDC measurements reveal that the dust flux around 50 AU is higher than predicted, indicating that Kuiper belt dust extend beyond the edge of the Kuiper belt.

This thesis aims to investigate the behaviour of dust grains that originate in the Kuiper belt, and the extension of the dust ring that these grains form, in order to explain the measurements conducted by SDC. A central aspect of this investigation is to explore the behaviour of water-ice in the Kuiper belt. Simulations of dust grain trajectories that are released from parent objects in the Kuiper belt are performed. The simulations consider grains that are composed of only silicate, and grains that have a mixed composition of silicate and water-ice. An important process that affects the dust is mass loss due to photosputtering, where photons collide with a grain causing the material to erode. For the first time in this thesis, the photosputtering rate is calculated for water-ice grains in the Solar System.

The results reveal that the presence of water-ice on Kuiper belt dust significantly influences the orbits of the grains, resulting in a more stable and confined dust ring in the Solar System, with distributions remaining closer to the parent objects compared to the pure silicate grains. However, it is seen that grains originating at approximately 43 AU have orbits that extend beyond the edge of the Kuiper belt, suggesting that dust grains observed beyond 50 AU can be Kuiper belt dust.

Acknowledgements

I would first and foremost like to thank my supervisor Professor Ingrid Mann for invaluable guidance through the entire process of this master's thesis, and for your continuous support and mentorship over the past years. A big thanks to Dr Andrew Poppe for all our discussions and for providing me with the necessary data to conduct this research. I am also grateful for warmly welcoming me to the University of California, Berkeley and making my stay there enjoyable and enlightening.

I want to thank Dr Audun Theodorsen and Samuel Kočiščák for our discussions, and for providing helpful comments and feedback on my work. A big thanks is owed to Professor Aigen Li for sharing data that has been used in this thesis.

Additionally, I am thankful to my fellow students for your support and encouragement, and for making the past five years an enjoyable experience.

Lastly I would like to thank my brother Erlend for answering any questions I had about Python and helping to make my code more efficient, and my father Rolf for proofreading this thesis.

Contents

List of Figures

List of Tables

1 Introduction

The Kuiper belt is located in the outer Solar System, and is a disk composed of icy objects. Within this region, dust grains are generated from Kuiper belt objects (KBOs) through collisions and fragmentations. The measurement of dust grains in the Kuiper belt is limited, but they have been measured for one of the first times by the ongoing New Horizons mission, as discussed in Poppe (2016). This is a spacecraft that has travelled through the Solar System and has recently passed the outer edge of the Kuiper belt at $\sim$ 50 AU. It has conducted in-situ measurements of the dust flux in the Solar System using the Student Dust Counter (SDC) instrument. The observations show an increase in dust impacts between 30 and 50 AU, which corresponds to the location of the Kuiper belt.

The SDC measurements indicates that the dust flux is higher than the prediction based on a model by Poppe (2016). The objective of this thesis is to investigate the behaviour of dust grains in the Kuiper belt, with the aim of explaining the measurements conducted by New Horizons SDC, as well as considering the future development of the dust flux as the spacecraft travels beyond the Kuiper belt. We want to determine the extension of dust grains that are produced in the Kuiper belt. This is done by performing simulations of dust grains originating in the Kuiper belt, and tracing the grains through their lifetimes.

The behaviour of the dust grains is dependent on their composition. Silicates are typical components of dust in the Solar System, but KBOs also have ice components. A central aspect of this investigation is examining the influence

of water-ice on the trajectory of the grains, and compare it to pure silicate grains.

Furthermore, this thesis considers the mass loss of water-ice grains due to photosputtering. The influence of mass loss is of interest because as a dust grain erodes, its trajectory will be influenced such that the grain is pushed further out in the Solar System. Mass loss is typically caused by sublimation and solar wind sputtering, which has been investigated by Mukai and Schwehm (1981). Grigorieva et al. (2007) considered the mass loss due to photosputtering of water-ice grains in other star systems, and found that this process is significant in the erosion of the water-ice. In this thesis photosputtering will be considered for the Solar System for the first time.

The thesis starts by providing the necessary background theory in Chapter 2 and laying the foundation for understanding the behaviour of dust grains in the Kuiper belt. Chapter 3 discusses the New Horizons observations and outlines the research questions and approach employed throughout the thesis. This is followed by a description of the method used to perform the simulations in Chapter 4, including initial calculations to formulate the hypothesis, computation of the photosputtering rate, and a detailed description of the model used to simulate dust grain trajectories. Chapter 5 presents the results of the simulations and provides an analysis of the dust grain behaviour. Finally, Chapter 6 offers a summary of the thesis and concludes the results.

2 Background

In this chapter, the theory used for simulations and analysis throughout the thesis is introduced. Initially the Kuiper belt will be discussed in Section 2.1, followed by a description of dust in the Kuiper belt in Section 2.2. In Section 2.3, the forces acting on dust particles in the Kuiper belt are explained. Further, the mass loss processes that influence the grains are discussed in Section 2.4.

2.1 Kuiper belt

The Kuiper belt is a disk consisting of icy objects that is located in the outer Solar System, and extends from 30 to approximately 50 AU from the Sun. When these icy objects come closer to the Sun, they can become comets. The Kuiper belt can be divided into subregions, where the classical Kuiper belt is located between $\sim$ 42 and $\sim$ 48 AU. This region can again be divided into the cold population, between 42.5 to 45 AU where the Kuiper belt objects (KBOs) have inclinations less than 4° relative to the ecliptic plane, and eccentricities less than 0.1, and the hot population, where objects have higher inclinations up to 30° and eccentricities up to 0.3 (Dawson and Murray-Clay, 2012).

The orbits of KBOs are, aside from the Sun, influenced by the outer planets. For distances less than $\sim$ 42 AU from the Sun and further out than approximately 48 AU, the KBOs are in mean-motion resonance with Neptune. Closer to the Sun than 42 AU, the KBOs experience a 2:3 resonance with Neptune, which

means that an object makes two orbits in the same time as Neptune makes three orbits around the Sun, and they have a synchronised motion. This resonance is centered around 39.4 AU, meaning the semi-major axis of the KBOs are at this distance from the Sun (Lykawka and Mukai, 2007). Further out than 47.5 AU, KBOs can be trapped in 1:2 resonance with Neptune, which corresponds to the objects making half an orbit each time Neptune makes one revolution around the Sun. This resonance corresponds to a semi-major axis of 47.8 AU (Lykawka and Mukai, 2007). KBOs can also be trapped in resonance with the other outer planets – Uranus, Saturn and Jupiter – but Neptune is the most efficient at capturing KBOs in a mean-motion resonance.

2.2 Dust in the Kuiper belt

Dust grains can be generated in the Kuiper belt by mechanisms such as mutual collisions between KBOs, and through the bombardment of interstellar dust on KBOs which causes dust to be ejected from the object. Interstellar dust (ISD) can enter the Solar System, and has been detected by the Ulysses and Galileo spacecraft, as discussed in Mann (2010). The sizes of ISD that have been measured are between $\sim$ 0.05 μm and $\sim$ 1 μm, but it is uncertain whether there are larger particles that enter the Solar System.

The newly generated dust grains will be released from the larger KBO, denoted in this thesis as the parent object of the dust grain. The surface structure of the KBOs is not well known, and it is uncertain what happens when they fragment. Furthermore, the size distribution of the produced grains is not known. KBOs can be composed of a mixture of silicates and water-ice. Dust grains that are produced from KBOs in the outer Solar System would have a water-ice component, and it is often assumed that these grains are core-mantle particles. They would have an ice mantle due to water recondensing onto the silicate core, or because the water-ice mantle is preserved following a collision (Grigorieva et al., 2007). Water-ice has been detected in the Solar System on satellite surfaces and on planetary surfaces, as well as in the gas cloud surrounding comets (Grigorieva et al., 2007).

2.3 Forces

After the grains are launched, the forces acting on the dust grains are gravity, radiation pressure, Poynting-Robertson drag, solar wind particle pressure, solar wind drag, and Lorentz force.

Gravity

Gravity is the force of attraction between two objects due to their mass. The force between two masses m and M is defined as

$$F_g = \frac{GMm}{r^2} \tag{2.1}$$

where G is the gravitational constant, and r is the distance between the two objects.

Radiation pressure

Radiation pressure is the force exerted on an object by electromagnetic radiation. When photons collide with an object, they can transfer momentum to the object, which causes it to be pushed in the direction of the photon velocity. The radiation pressure is dependant on the solar irradiance, and the scattering and absorption properties of the object. Assuming we have a spherical particle, it can be written as

$$F_{rad} = \frac{\pi a_d^2}{c} S Q_{pr} \tag{2.2}$$

where a_d is the radius of the grain, c is the speed of light, and S is the radiation flux density, defined as $S = L_\odot/(4\pi r^2)$, in which $L_\odot$ is the solar luminosity, and r is the distance from the Sun. The radiation pressure coefficient Q_{pr} is a measure of the amount of energy that is absorbed by the grain, and depends on the grains' physical properties and the wavelength of incoming radiation (Burns et al., 1979). This force works in the radial direction. The radiation pressure force is significant for smaller grains, but becomes less important for grains of larger sizes.

β-value

The force of gravity F_g and radiation pressure force F_{rad} are both radial forces that scale with $1/r^2$, and it is useful to discuss the ratio between these two forces, defined as the β-value of the grain,

$$\beta = \frac{F_{rad}}{F_g} \tag{2.3}$$

This value will influence the orbit of an object, and be a contributing factor to whether it will stay in bound or unbound orbit. If we insert equation 2.1 and 2.2, and assume a spherical particle with radius a_d and mass density ρ in cgs units, the β-value becomes (Burns et al., 1979)

$$\beta = \frac{F_{rad}}{F_g} = \frac{3L_\odot}{16\pi G M_\odot c} \frac{Q_{pr}}{\rho a_d} \tag{2.4}$$

where $M_\odot$ is the mass of the Sun. The β-value is independent of distance to the Sun, and aside from the solar luminosity, it is only a function of the composition and size of the particle.

Poynting-Robertson drag

Poynting-Robertson drag is the tangential component of the radiation pressure force, in the frame of a moving particle, and works in the direction opposite to the dust grain velocity. This drag force is caused by the absorption and re-radiation of solar radiation by the particle. As a result, the particle loses angular momentum and orbital energy, and is decelerated, which causes the particle to slowly spiral inward towards the star. Poynting-Robertson drag is a very small effect, and is most noticeable for small particles or dust grains, which have a large surface area to mass ratio.

Solar wind particle pressure

Solar wind particle pressure refers to the force exerted on objects in interplanetary space due to the momentum flux carried by the solar wind. The solar wind force is given by

$$F_{sw} = \sum_i \rho_i v_{sw}^2 C_{sw,i} \tag{2.5}$$

where ρ_i is the mass density of the i-th solar wind particle species, v_{sw} is the solar wind speed, and $C_{sw,i}$ is the momentum transfer cross section (Minato et al., 2004). The solar wind particle pressure works in the radial direction of the object.

Solar wind drag

Solar wind drag is the tangential component of the solar wind particle pressure, and acts in the direction opposite to the dust grain velocity. It is an effect that causes objects in space to decelerate, as the solar wind collides with an object and transfers momentum to the particle. Similarly to the Poynting-Robertson drag, the solar wind drag will cause a particle to loose orbital energy and spiral towards the star. The magnitude of the solar wind drag depends on the solar wind density, the surface area of the object, and the relative velocity between the object and the solar wind. This force becomes significant at small grain radii, approximately < 0.1 μm. In the size range of 1 μm and larger, this force is approximately constant with size, and can be considered to be independent of the radius (Minato et al., 2004).

Lorentz force

Lorentz force is the force that a charged particle experiences when moving in an electromagnetic field, and it is given by

$$\boldsymbol{F}_L = q(\boldsymbol{E} + \dot{\boldsymbol{r}}_s \times \boldsymbol{B}) \tag{2.6}$$

where q is the charge of the particle, $\dot{\boldsymbol{r}}_s$ is the velocity of the particle, $\boldsymbol{E}$ is the electric field, and $\boldsymbol{B}$ is the magnetic field. The magnetic field will cause the charged particle to move in a cyclotron motion, since the cross product $\dot{\boldsymbol{r}}_s \times \boldsymbol{B}$ is perpendicular to to the velocity and the magnetic field. This can cause the particles to be pushed to higher or lower inclinations relative to the orbit plane. For particles with low charge, the Lorentz force is not significant in comparison to the other forces acting on a dust grain.

2.4 Mass loss processes

Dust grains in the Kuiper belt are subject to mass loss processes, such as charged particle sputtering, sublimation, and photosputtering. In this section these three mass loss processes are discussed, since they are incorporated in the model used for simulating dust grain trajectories.

Photosputtering

Photosputtering is the process where a solid material is eroded by the impact of UV photons. A dust grain can absorb the photons, which can cause the atoms or molecules on the surface of the material to become excited or ionized, leading to their ejection from the surface. In the case of water-ice grains, the water molecules on the dust grain surface can be dissociated by a UV photon. The OH^- fragment can be desorbed, or the molecule can recombine and then either leave the surface of the grain, or transfer momentum to a neighbouring molecule which then may leave the surface (Grigorieva et al., 2007).

The erosion rate due to photosputtering for an icy grain is given by (Grigorieva et al., 2007):

$$\dot{s}_{ps} = -\frac{\eta m_{H_2O} Y_{ps} N_{abs}}{4\rho} \tag{2.7}$$

where m_{H_2O} is the mass of a water molecule, ρ is the mass density of the grain, η is the fraction of the grain's surface covered in ice, Y_{ps} is the photosputtering yield which depends weakly on the grain temperature and the absorbed photon

wavelength, and N_{abs} is defined as

$$N_{abs} = \int_{\lambda_{min}}^{\lambda_{max}} \frac{F(r,\lambda)}{hc/\lambda} Q_{abs}(\lambda) d\lambda \tag{2.8}$$

and is the number of absorbed photons. Here $F(r,\lambda)$ is the incident stellar flux as a function of wavelength λ at a distance r from the star. The stellar flux is to first order inversely proportional to the square of the distance. Further, Q_{abs} is the absorption coefficient for water-ice surfaces which depends on the energy of the incident photon and the size of the dust grain, and λ_{min} and λ_{max} are respectively the minimum and maximum wavelengths corresponding to the energy of sputtering photons (Grigorieva et al., 2007).

Sublimation

Sublimation is a process in which a substance transitions directly from the solid phase to the gas phase. It occurs when the vapour pressure of a solid substance exceeds the atmospheric pressure at its surface temperature. The molecules at the surface of the solid absorb energy from their surroundings, and gain enough energy to overcome the intermolecular bond that bind them in the solid phase and transitions into gas phase. For icy bodies, solar radiation causes them to heat up, which leads to the ice on the surface sublimating. This can lead to erosion or structural changes of the icy body, since the sublimation of surface material can weaken or remove the outer layers of the body.

The mass loss rate per unit area due to sublimation in interplanetary space is (Mukai and Schwehm, 1981):

$$\frac{dm}{dt} = 10^8 \frac{E_s}{4\pi L a_{\mu m}^2} \tag{2.9}$$

in units of g cm^{-2} s^{-1}. Here L is the latent heat of sublimation in units of erg g^{-1}, $a_{\mu m}$ is the radius of the grain in μm, and E_s is the energy loss function due to sublimation in units of erg s^{-1}, given by (Mukai and Schwehm, 1981)

$$E_s = 5.5 \times 10^{-12} \sqrt{\frac{\mu}{T_g}} a_{\mu m}^2 L \ \exp\left(-1.2 \times 10^{-8} \frac{\mu L}{T_g} + b(T_g)\right) \tag{2.10}$$

where μ is the average molecular weight of the evaporated molecules, T_g is the grain temperature, and $b(T_g)$ is a function that depends on the composition and temperature of the grain. For water-ice this function is defined as

$$b(T_g) = 8.88 \log(T_g) + 7.85 \times 10^{-3} T_g + 1.12 \times 10^{-7} T_g^2 + 9.98 \tag{2.11}$$

The mass loss rate can be converted to radius loss rate by:

$$\dot{s}_{sub} = -\frac{1}{4\pi\rho a_{\mu m}^2} 4\pi(a_d \times 10^{-4})^2 \frac{dm}{dt} \tag{2.12}$$

in units of cm s^{-1}. The factor $4\pi(a_d \times 10^{-4})^2$ comes from converting mass loss per unit surface area to mass loss rate for specific grain size, where a_d is the radius in m.

Charged particle sputtering

Charged particle sputtering occurs when an object, e.g. a dust grain, is bombarded by high-energy particles, like solar wind ions. When the incident charged particle collides with the target material, it transfer some of its energy and momentum to the target atoms or molecules, causing them to be ejected from the solid. Sputtering is characterized by a sputtering yield Y, which is the number of atoms or molecules ejected per incident particle. This yield depends on the energy and angle of incidence of the high-energy particles, and the mass, composition, and properties of the target material (Mukai and Schwehm, 1981).

The radius loss rate in units of cm s^{-1} due to charged particle sputtering is

$$\dot{s}_{sput} = -\frac{m}{\rho}(f_p Y_p + f_\alpha Y_\alpha) \tag{2.13}$$

where m is the mass in units of g, and ρ is the mass density of the material in g cm^{-3}, f is the flux of the incident particle species, and Y is the sputtering yield. The subscripts p and α denote proton and α-particles, respectively. The charged particle sputtering, similarly to photosputtering, is inversely proportional to r^2.

The proton flux is

$$f_p = \frac{f_{sw}(1 - sw_\alpha)}{\sqrt{r}}$$

and the α flux is

$$f_\alpha = \frac{sw_\alpha f_{sw}}{\sqrt{r}}$$

where r is the heliocentric distance in AU, f_{sw} is the solar wind flux at 1 AU from the Sun per cm^3 per second, and sw_α is the fraction of α particles in the solar wind.

3

New Horizons observations and research approach

New Horizons is a spacecraft that has travelled through the Solar System, and has reached a distance of 55 AU from the Sun as of 2023. One of the instruments on the spacecraft is the Student Dust Counter (SDC), which is an in situ dust detector that is sensitive to dust grains with radius $0.5 < a_d < 5$ μm (Poppe, 2016). The SDC has conducted measurements of the dust flux through the Solar System, and this is shown in Figure 3.1. The blue points are the SDC measurements, and the red curves show the predicted dust flux using a model by Poppe (2016). The dotted curve assumes only impacts from interstellar dust, the solid curve shows the estimated impacts from Kuiper belt dust, and the dashed curve is the estimation assuming impacts from both interstellar dust and Kuiper belt dust. As can be seen, the model predicts that the dust flux will decrease beyond 42 AU. However, the SDC measurements show an increasing dust flux beyond this distance, and a higher flux than predicted around 50 AU.

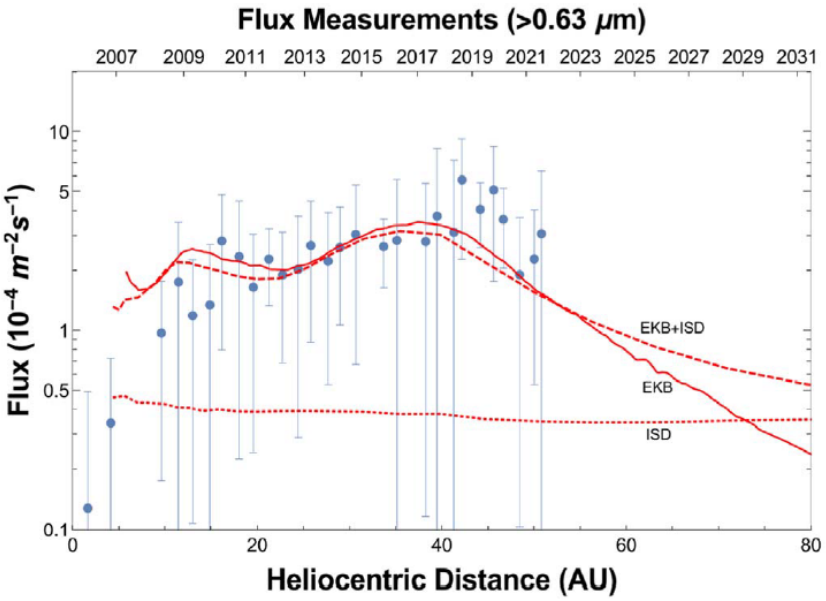

Figure 3.1: Dust flux onto the New Horizons SDC. The blue points are the measurements made by the spacecraft, and the red curves are the estimated fluences assuming interstellar dust (ISD), Kuiper belt dust (EKB), and a combination of both. The figure is taken from Bernardoni et al. (2022).

The investigation presented in this master's thesis focuses on understanding the deviation between the measured dust flux by the SDC and the predicted flux, as shown in Figure 3.1, and examining how the measurements will develop in the future. The thesis aims to investigate whether the orbits of Kuiper belt dust can explain the observations made by the SDC. This is done by simulating dust grains that originate in the Kuiper belt to examine how far out the Kuiper belt dust extends in the Solar System. If the Kuiper belt grains remain within 50 AU, then the dust observed beyond this distance would be interstellar dust.

The extension of the dust ring in the Kuiper belt is often assumed to be equivalent to that of the Kuiper belt itself. However, in Section 2.3 we presented the forces acting on the Kuiper belt dust, and it is clear that there are size-dependent forces acting on the grains, aside from the force of gravity. In particular, the radiation pressure force is more significant for smaller particles, and this force will push the smaller grains out on more elliptical orbits, so the dust ring from the smaller grains will have a wider extension.

One possible factor contributing to the deviation of the modelled and measured dust flux is the presence of water-ice grains in the Kuiper belt, which was not considered in the model used in Figure 3.1. In order to have a quantitative

description of grains that include both silicate and water-ice, a core-mantle assumption is adopted. This assumes that the grains have a silicate core with an outer mantle of water-ice. We will simulate both core-mantle grains and pure silicate grains, in order to investigate the difference in behaviour between the grain compositions.

The initial considerations are based on calculations conducted by Grigorieva et al. (2007), who investigated water-ice grains in debris disks around stars. These are disks of dust particles that are produced by colliding planetesimals. In the paper they calculated the erosion rate of the grains due to photosputtering, and found that this mass loss process is significant in the erosion of water-ice grains. The mass loss of a grain is of interest, since it can have a considerable effect on the behaviour of the grains and contribute to a wider extension of the dust ring in the Kuiper belt. As a grain loses mass, the β-value becomes higher, and the particle will be pushed further out in the Solar System. If the erosion rate is high, then this could be a possible reason the flux is higher than predicted in the outer edge of the Kuiper belt. In this thesis, we calculate for the first time the photosputtering rate of water-ice grains in the Solar System.

To simulate dust grains generated in the Kuiper belt, a detailed model developed by Poppe (2016) is employed, which solves the equation of motion of a dust grain. The model has previously considered silicate grains and accounted for the erosion due to solar wind sputtering and sublimation. In this thesis, the model is adapted to consider core-mantle grains, and the mass loss due to photosputtering is incorporated into the model for the first time. The trajectories of numerous dust grains will be calculated using this model, aiming to compare and analyse the differences in behaviour between the mixed composition grains and pure silicate grains.

In that regard we want to make initial calculations of how the trajectories of water-ice grains differs from silicate grains. This is done by comparing the β-value for water-ice and silicate, and computing the semi-major axis and orbits for the two compositions using Kepler's equation, taking into account only radiation pressure force and force of gravity.

This thesis aims to provide an understanding of the discrepancies observed between the measured and predicted dust flux by the SDC on New Horizons. We want to investigate the role of water-ice particles, the influence of photosputtering, the extension of the dust ring in the Solar System, and ultimately contribute to our understanding of the behaviour of Kuiper belt dust.

4

Method

In this chapter, we start by presenting the initial calculations conducted by assuming only gravitational force and radiation pressure force are acting on the grains, described in section 4.1. Section 4.2 presents the computation of the photosputtering rate for water-ice grains in the Solar System. This is followed by a description of the model used to simulate the dust grains in the Kuiper belt in section 4.3. In section 4.4, we discuss how the orbital elements are computed based on the model output.

4.1 Single particle calculations using gravity and radiation pressure

4.1.1 Comparison of β-values for different particle compositions

The β-value is the ratio of the radiation pressure force to gravitational force, as defined in Section 2.3. This ratio is independent of distance to the Sun, but depends on the radius and mass density of the dust grain. As the water-ice mantle on a grain erodes, the radius of the grain will decrease, leading to a change in β-value and a change in the orbit of the grain. Figure 4.1 shows the β-value as a function of radius for water-ice grains. The data is from Li (2023).

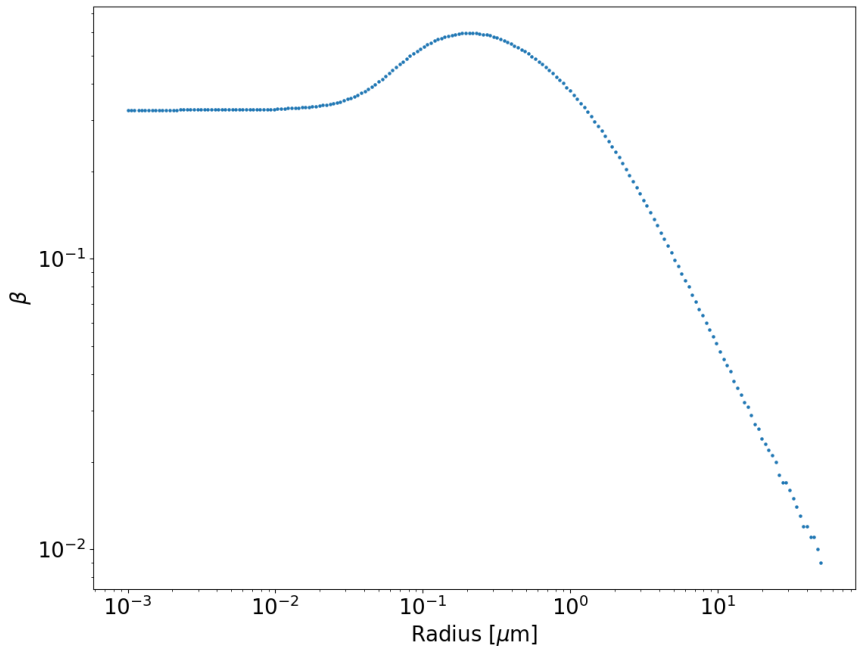

Figure 4.1: β-value as a function of radius for water-ice grains.

The composition of the dust grains will also affect the β-value, since it is dependent on the mass density and optical properties of the material. Figure 4.2 shows the β-values for different grain compositions, for particles with radii $1 < a_d < 10$ μm. The comparison includes the β-values for asteroidal grains, with values taken from Wilck and Mann (1996), and the values for water-ice grains, obtained from Li (2023). Furthermore, the β-values calculated using equation 2.4, assuming a mass density of $\rho_{sil} = 2$ g cm^{-3} are also included in the figure, which is the equation that will be used in the model when simulating the grains. It is evident from the figure that the water-ice grains have a higher β-value than the asteroidal grains.

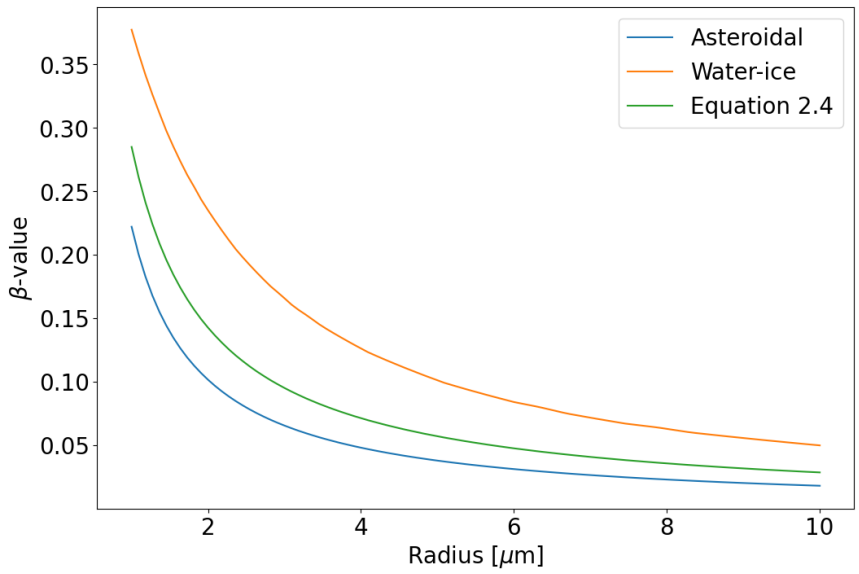

Figure 4.2: Comparison of the β-value as a function of radius for asteroidal grains, water-ice grains, and when computing it using equation 2.4.

4.1.2 Effect of β-value

In the case when the only forces acting on the grains are gravity and radiation pressure force, the β-value will determine the behaviour of the dust orbits. A change in β-value will lead to a change in the semi-major axis. Assuming a grain is launched from a parent object with eccentricity $e_{parent} = 0$ and semi-major axis $a_{parent} = 40$ AU, the semi-major axis of the grain can be computed by

$$a_{sma} = \frac{r\mu(1-\beta)}{2\mu(1-\beta) - rv^2} \tag{4.1}$$

where $\mu = GM_{\odot}$ is the gravitational parameter, r is the heliocentric distance where the grains are launched, and v is the velocity of the parent object. Figure 4.3 shows the semi-major axis when using the β-values for asteroidal grains, water-ice grains, and computed using equation 2.4. Since water-ice grains have higher β-values than asteroidal grains, the semi-major axis for water-ice is also higher as a function of the radius. The difference between the two compositions become less significant at higher radii.

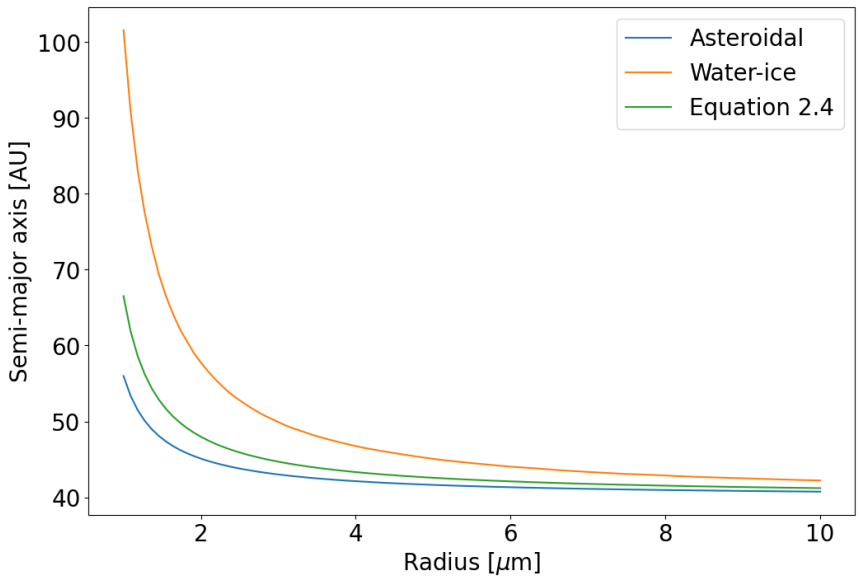

Figure 4.3: Comparison of the semi-major axis when using β-values of asteroidal grains, water-ice grains, and when computing it using equation 2.4.

To investigate the impact of the β-value on the trajectories of dust grains, we compute the orbits of grains upon their release from a parent object, using the three β-value assumptions. This is calculated by solving Kepler's equations, modified to include the radiation pressure force. The heliocentric distance can be computed by (Fortescue et al., 2011):

$$r = a_{sma}(1 - e\cos E) \tag{4.2}$$

where e is the eccentricity and E is the eccentric anomaly, which can be solved by Kepler's equation, for an orbit with eccentricity $0 < e < 1$:

$$M = E - e\sin E \tag{4.3}$$

where $M = nt$ is the mean anomaly, which is dependent on the mean-motion

$$n = \sqrt{\frac{\mu(1-\beta)}{(-a_{sma})^3}} \tag{4.4}$$

The orbits are computed for grains with radius of 1 μm and 10 μm. These are shown in Figure 4.4, and from both figures it can be seen that the water-ice grains have orbits that extend further out in the Solar System compared to the asteroidal grains. For a 1 μm particle, this difference is significant, whereas for the 10 μm grain the difference is quite small, but still present. These calculations are an approximation assuming a two-body problem with the influences

of gravity and radiation pressure from the Sun. When including additional forces acting on the grains, the behaviour of the dust orbits will no longer be determined by the β-value alone. However, these preliminary results lead to the expectation that the water-ice grains will have a higher semi-major axis compared to the pure silicate grains, and consequently they are expected to travel further out in the Solar System.

Another thing to note is how the β-value for a 1 μm particle is higher than for the 10 μm particle, and the radiation pressure force causes the smaller grains to be pushed further out in the Solar System. The significance of this is that grains that are launched with a radius of 10 μm will remain on an orbit close to the parent object. However, a grain launched with a radius of 1 μm will immediately be pushed onto a more elliptical orbit by the radiation pressure force.

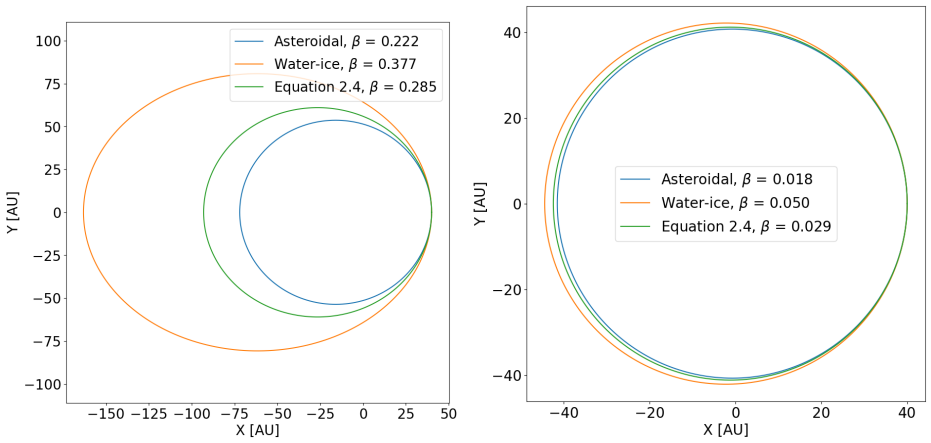

(a) r=1 μm **(b)** r=10 μm

Figure 4.4: Grains launched from a parent object on circular orbit at a distance of 40 AU from the Sun.

4.2 Photosputtering rates

A central focus in this thesis is the mass loss due to photosputtering. Mass loss from charged particle sputtering and sublimation have been computed in multiple previous studies, see for example Mukai and Schwehm (1981) and Baumann et al. (2020), while photosputtering is an effect that has not been considered in detail for the Solar System. The purpose of this section is to compute the photosputtering rate of water-ice grains in the Kuiper belt.

The computation of the photosputtering is based on the theory and calculations

made by Grigorieva et al. (2007). They define the equation for the photosputtering rate, given in equation 2.7, and give the erosion rate for multiple star systems and debris disks. The star that is of interest is the Sun, which is a G-type main sequence star. Table 4.1 shows the erosion rates and photosputtering lifetimes of the two G-type stars that are provided in Grigorieva et al. (2007), at a distance of 100 AU from the star.

The values presented in the table show that a G0V and a G2V type star causes the same erosion rate, indicating that the stellar flux for the two stars are identical. However, these two stars have effective temperatures of $T_{G0V} = 5920$ K and $T_{G2V} = 5770$ K (Pecaut and Mamajek, 2013), and in Figure 4.6 the blackbody spectra for these two star types are shown. It is evident that a G0V star at higher temperature emits a greater stellar flux, and consequently it is expected that the photosputtering rate will be lower for a G2V type star. To validate the rates given in Table 4.1, we will perform calculations of the photosputtering rates for the two star types.

Name	Type	$\dot{s}_{ps}$ [μm yr^{-1}]	t [yr]
HD 1581	G0V	10^{-6}	2×10^7
HD 20807	G2V	10^{-6}	2×10^7

Table 4.1: Photosputtering rates for the G-type stars, and the grain lifetime of a 20 μm particle, at a distance of 100 AU from the star. Values taken from Grigorieva et al. (2007).

To calculate the photosputtering rate, as defined in equation 2.7, information on both the stellar flux $F(r, \lambda)$ and the absorption coefficient Q_{abs} is required. Initially, the absorption coefficient provided by Grigorieva et al. (2007) is used, and this is shown in Figure 4.5. We compute the erosion rate for a G0V and a G2V type star using their respective blackbody spectra at a distance of 100 AU from the star, in order to compare to the values in Table 4.1. Additionally, the erosion rate is calculated using the solar spectrum, since it is of interest to know the rate in the Solar System, as this will be used in later calculations.

Furthermore, it is necessary to define the remaining parameters in equation 2.7. It is assumed that the photosputtering yield remains constant with a value of $Y_{ps} = 10^{-3}$. This is chosen based on estimates from Andersson et al. (2006) and Westley et al. (1995). Andersson et al. (2006) found that the lowest value for the photosputtering yield was 4×10^{-4} for amorphous ice, and Westley et al. (1995) found that the highest Y_{ps} was 7×10^{-3} for temperatures above 100 K. Therefore the chosen value for the UV sputtering yield is an intermediate value between these two extremes, $Y_{ps} = 1 \times 10^{-3}$. It is assumed to be constant, since the yield is only weakly dependent on temperature and the absorbed photon

wavelength (Grigorieva et al., 2007).

As we assume that the grains have a water-ice mantle, the fraction of the dust surface covered in ice is $\eta = 1$. The mass of a water molecule is $m_{H_2O} = 3 \times 10^{-23}$ g and the mass density of water-ice is $\rho = 917$ kg/m^3. The minimum and maximum wavelengths are taken to be $\lambda_{min} = 0.091$ μm and $\lambda_{max} = 0.24$ μm, respectively. The maximum wavelength of 0.24 μm corresponds to an energy of 5.1 eV, which is the dissociation energy of the O-H bond, and is chosen since the desorption is triggered by the dissociation of a water molecule (Grigorieva et al., 2007). The minimum wavelength corresponds to an energy of 13.6 eV, which is the upper energy limit considered for this process.

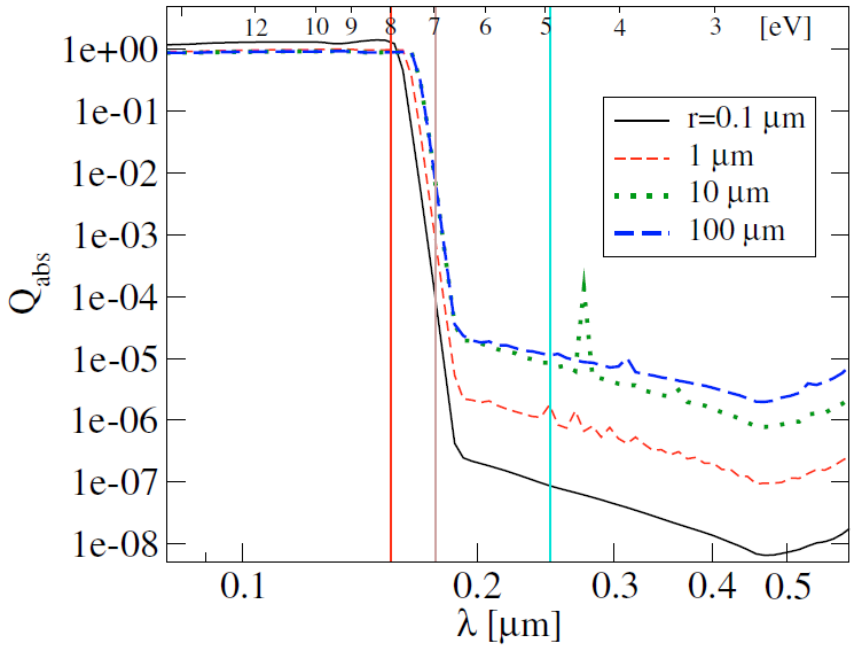

Figure 4.5: The absorption coefficient Q_{abs} for different grain sizes of water-ice particles. The figure is taken from Grigorieva et al. (2007).

Varying the stellar flux

We compute the blackbody spectra for a G0V and G2V type star, and extrapolate them to a distance of 100 AU from the star – this is plotted in Figure 4.6. The figure also shows the solar spectrum at a solar minimum and maximum, with data taken from the National Centers for Environmental Information (NCEI) (Coddington et al., 2023), and extrapolated to 100 AU.

When using a blackbody spectrum for a G0V type star with temperature $T_{G0V} = 5920$ K as the stellar flux $F(R, \lambda)$, we find using equations 2.8 and 2.7 that the photosputtering rate is $\dot{s}_{G0V} = 8.56 \times 10^{-6}$ μm yr^{-1} at 100 AU. For a G2V type star, like the Sun, with an effective temperature of $T_{G2V} = 5778$ K, the photosputtering rate is $\dot{s}_{G2V} = 5.84 \times 10^{-6}$ μm yr^{-1} at 100 AU. Both of these values are computed using the absorption coefficient in Figure 4.5 for a 10 μm particle. As presented in Table 4.1, the values computed in Grigorieva et al. (2007) are 10^{-6} μm yr^{-1}, so they are on the same order of magnitude. The reason we get slightly different values could be due to the fact that the fluences are approximated to blackbody spectra. In addition, the temperatures are assumed based on typical G0V and G2V type stars, but even within a spectral class the temperature can vary. However, the computations show that the G2V type star will have a lower photosputtering rate.

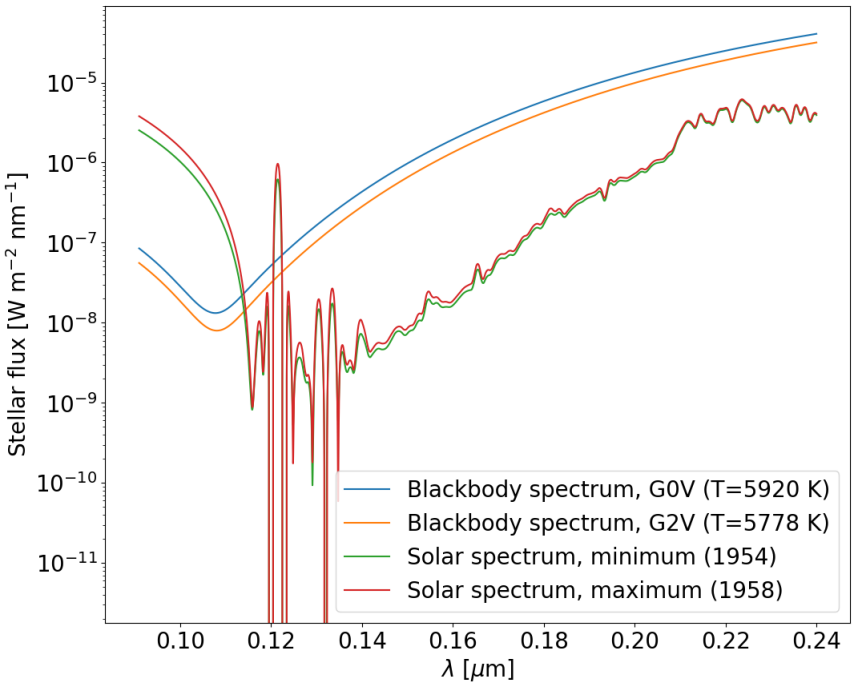

Figure 4.6: Comparison of the blackbody spectrum for a G0V star and a G2V star, and the solar spectrum in a year of solar maximum and solar minimum. The fluences are calculated at a distance of 100 AU from the star.

Varying the absorption coefficient

To accurately compute the photosputtering rate for a range of dust grain radii, we require the absorption coefficient for more grain sizes than what is provided in Figure 4.5. From Li (2023) we received the absorption coefficient for water-

ice grains of different radii, which are shown in Figure 4.7. Using the new absorption coefficient, we initially compute the photosputtering rate for a 10 μm grain at a distance of 100 AU. Employing the blackbody spectra for a G0V type star, the computed photosputtering is $\dot{s}_{G0V} = 3.51\times10^{-4}$ μm yr^{-1}, and for a G2V type star, we find the rate to be $\dot{s}_{G2V} = 2.66\times10^{-4}$ μm yr^{-1}. These values, together with the erosion rates computed using the Q_{abs} from Grigorieva et al. (2007) are summarised in Table 4.2. Also included in the table are the erosion rates calculated for both absorption coefficients, using the solar spectra data from NCEI at solar minimum and maximum.

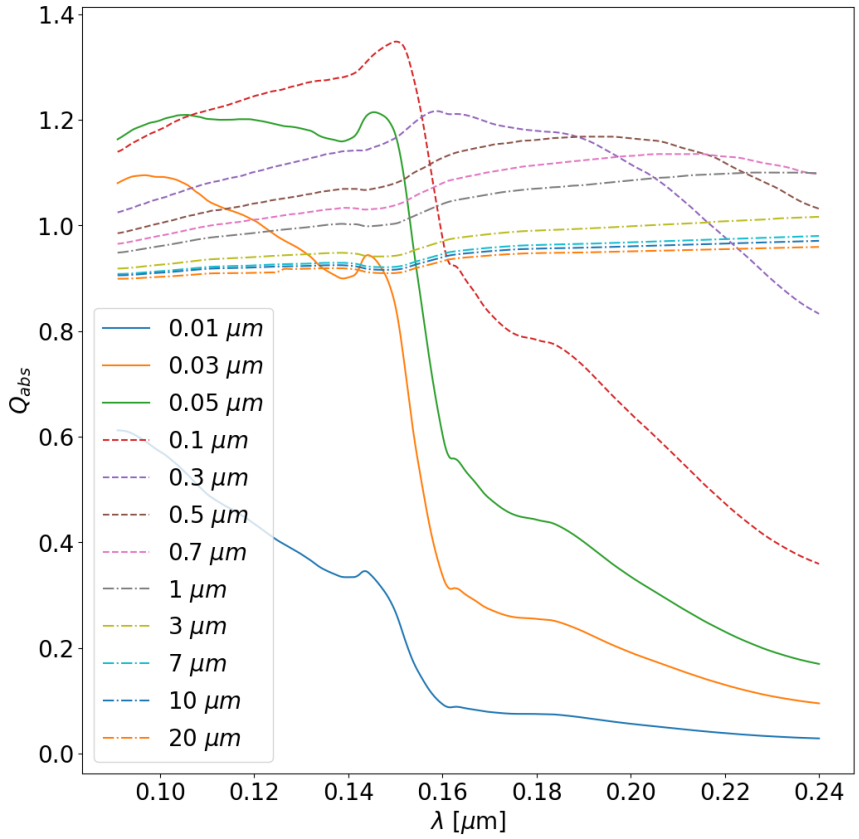

Figure 4.7: Absorption coefficient for water-ice particles of different radii, as a function of wavelength. Data are from Li (2023).

Stellar flux	$\dot{s}_{ps}$ [μm yr^{-1}] (Grigorieva)	$\dot{s}_{ps}$ [μm yr^{-1}] (Li)
Blackbody G0V	8.56×10^{-6}	4.51×10^{-4}
Blackbody G2V (Sun)	5.84×10^{-6}	2.66×10^{-4}
Solar spectrum, minimum	2.52×10^{-6}	4.16×10^{-5}
Solar spectrum, maximum	3.76×10^{-6}	4.46×10^{-5}

Table 4.2: Photosputtering rates for a 10 μm water-ice grain. We have compared the rates calculated by using the Q_{abs} from Grigorieva et al. (2007) and the Q_{abs} from Li (2023). These rates are at a distance of 100 AU from the star.

From Table 4.2 we can see that there is a significant difference between the photosputtering rates derived using the absorption coefficient from Grigorieva et al. (2007) and from Li (2023). Comparing the coefficients from Figure 4.5 and 4.7, it is clear that they are considerably different. The values from Li (2023) are more dependent on the size of the grain, whereas the coefficient used by Grigorieva et al. (2007) exhibit a lower dependence on the grain radii. In Figure 4.8 we have plotted the difference between the coefficients for a 10 μm water-ice grain, and it becomes apparent why the photosputtering rates are different.

The discrepancy in the coefficients arises from the way they were derived. Grigorieva et al. (2007) adopted an index of refraction for water-ice that was obtained from Artymowicz (1988). This index was chosen assuming liquid water, which is highly transparent. This is why the absorption coefficients from Grigorieva et al. (2007) have low values at wavelengths $0.2 < \lambda < 0.5$ μm, as seen in Figure 4.5. However, the coefficient by Li (2023) assumes that the water-ice has inclusions and is more absorbing than liquid water, which is a more reasonable assumption as it is unlikely that water-ice is transparent.

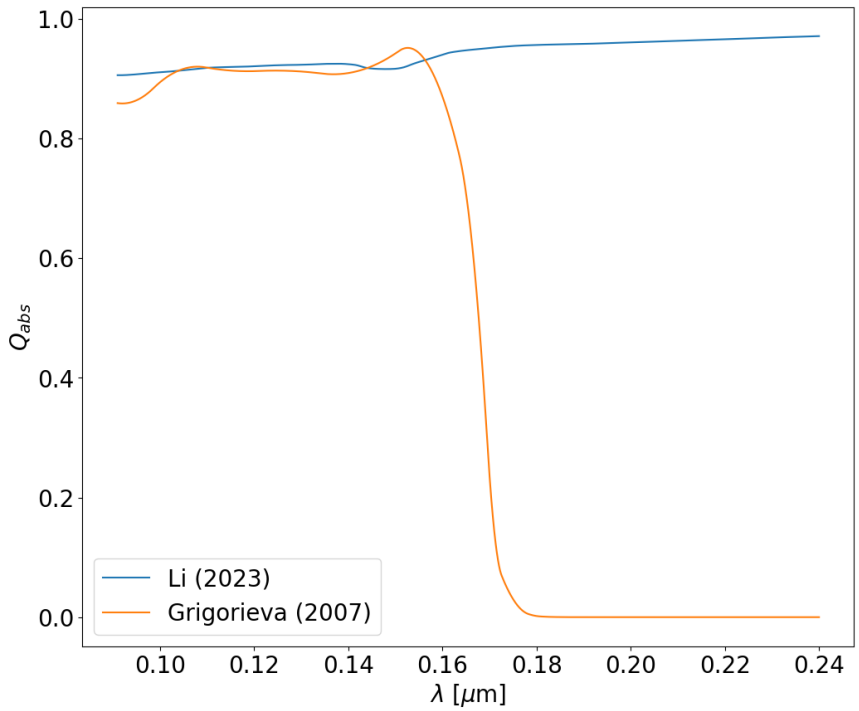

Figure 4.8: Comparison of the absorption coefficients from Li (2023) and Grigorieva et al. (2007) for a 10 μm water-ice grain.

Photosputtering rate for Kuiper belt grains

So far we have calculated the photosputtering rate for a 10 μm grain at a distance of 100 AU, but we are interested in the rates for a range of grain radii. Using the absorption coefficient given by Li (2023) as shown in Figure 4.7, and the stellar flux for both solar minimum and solar maximum, displayed in Figure 4.6, we compute the photosputtering rate for various grain sizes. The erosion rate as a function of dust grain radius is shown in Figure 4.9 at a distance of 1 AU from the Sun, and the data is provided in Table B.1 in the appendix. It is computed at this distance, since the erosion rate at 1 AU will be incorporated into the model for simulating the dust grains.

The dust grain sizes of interest are in the range $1 < r < 100$ μm, which is in the part of the curve where $\dot{s}_{ps}$ mostly flattens out and can be approximated as constant. Depending on the grain size and whether we have a solar maximum or solar minimum, the photosputtering rate at 1 AU is between 0.4 and 0.5 μm yr^{-1} for the size interval of interest, as can be seen from Figure 4.9. Thus, when simulating dust grains using the model described below in Section 4.3, we will use a constant photosputtering rate of $\dot{s}_{ps} = 0.4$ μm yr^{-1} at a distance

of 1 AU from the Sun.

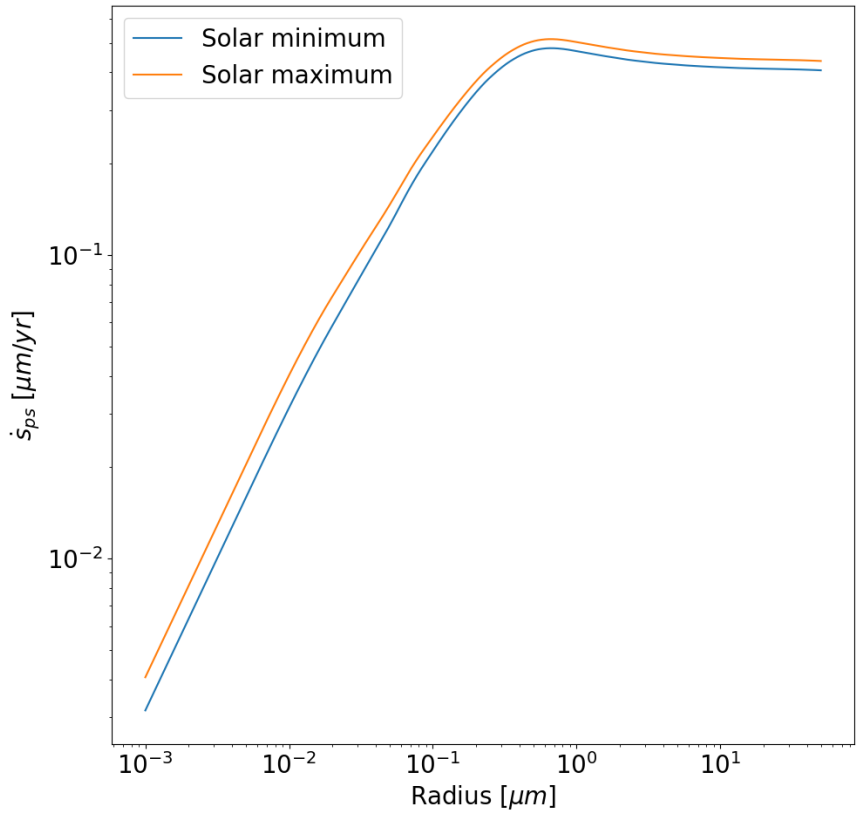

Figure 4.9: Photosputtering rate as a function of dust grain radius, plotted when using the solar spectral irradiance during both solar minimum and maximum at a distance of 1 AU from the Sun.

4.2.1 Comparison to charged particle sputtering and sublimation

To determine the significance of photosputtering compared to other mass loss processes, we compare the photosputtering rate to erosion due to solar wind sputtering and sublimation. Figure 4.10 is taken from Mukai and Schwehm (1981) and shows the solar wind sputtering lifetime and sublimation lifetime of magnetite and water-ice particles. The thin solid lines represents the solar wind sputtering lifetimes, and the dotted curves show the sublimation lifetimes. It can be seen that a 20 μm water-ice grain will have a solar wind sputtering lifetime of approximately $\sim 2\times10^{13}$ seconds, or 6.3×10^{5} years at a distance of 10 AU from the Sun. Extrapolating this to 1 AU, the lifetime becomes 6.3×10^{3} years.

We found that the photosputtering rate for the Sun at 1 AU is 0.4 μm yr^{-1}, and from that we have that the lifetime of a 20 μm grain would be 50 years. Both sputtering rates scale with $1/r^2$, and therefore it is sufficient to consider the erosion rates at 1 AU. The erosion due to photosputtering is thus more than 120 times faster than the erosion due to solar wind sputtering for water-ice grains.

Figure 4.10 shows the sublimation lifetime in the dotted lines. At 1 AU, a 20 μm water-ice grain has a sublimation lifetime of approximately 10^7 seconds, or 0.32 years. This is more than 150 times faster than the erosion due to photosputtering. However, beyond the snow line, the water-ice will not sublimate, and KBOs lie well beyond this boundary. Therefore, the most significant mass loss process for water-ice grains in the Kuiper belt is photosputtering.

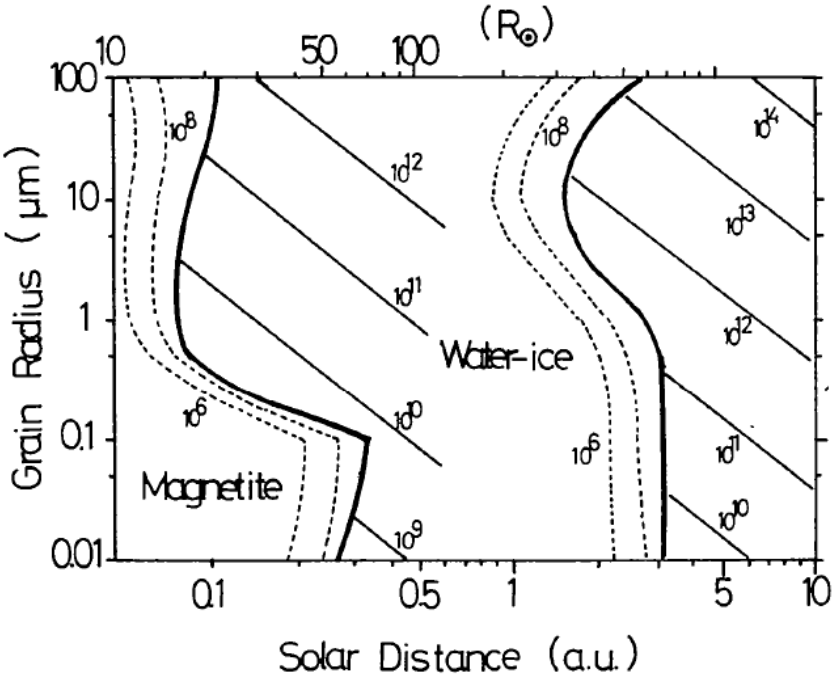

Figure 4.10: Lifetimes of magnetite and water-ice grains. The thin solid lines give the solar wind sputtering, and the dotted curves show the sublimation lifetime in units of seconds. This figure is taken from Mukai and Schwehm (1981).

4.3 Model for simulating dust grains

This section describes the model by Poppe (2016) that is used for simulating dust grain trajectories, and is implemented in a code at University of California, Berkeley. To begin the simulation, the grains are launched from parent bodies with initial conditions that correspond to the dynamically cold population of the Kuiper belt. This means the grains are launched with the velocity of the parent bodies, and have an initial semi-major axis between 42.5 and 44.5 AU, with orbital eccentricities between 0 and 0.1, and with inclinations less than 10 degrees relative to the ecliptic plane. The initial conditions are chosen randomly by a Monte Carlo approach (Poppe, 2023).

The dust grains that are generated will be subject to the forces described in Section 2.3. The following equation of motion is used in this model to describe the behaviour of an individual dust grain (Poppe, 2016):

$$\begin{aligned}\ddot{\boldsymbol{r}}_s = &-\frac{GM_\odot}{R_s^3}\boldsymbol{r}_s - \sum_{i=1}^{4}\frac{GM_i}{r_i^3}\boldsymbol{r}_i + \frac{1}{m}\boldsymbol{F}_L \\ &+ \frac{\pi a_d^2}{mc}SQ_{pr}\left[\left(1-(1+w)\frac{\dot{r}_s}{c}\right)\hat{\boldsymbol{r}}_s - (1+w)\frac{\dot{\boldsymbol{r}}_s}{c}\right]\end{aligned} \tag{4.5}$$

Here $\ddot{\boldsymbol{r}}$, $\dot{\boldsymbol{r}}$ and $\boldsymbol{r}$ are the acceleration, velocity and position vectors of the dust grain, $\hat{\boldsymbol{r}}$ is its unit vector, and the subscript s denotes with respect to the Sun, and i is with respect to the outer giant planets. G is the gravitational constant, $M_\odot$ and M_i are the masses of the Sun and the planets, respectively, m is the mass of the dust grain, and r_s and r_i are the distances to the Sun and to the planets. The other parameters are explained below.

The first two terms in equation 4.5 are the influence of gravity due to the Sun and the outer planets, i.e. Jupiter, Saturn, Uranus and Neptune. The third term represents the influence of the electromagnetic field, where $\boldsymbol{F}_L$ is the Lorentz force, as defined in equation 2.6. It is assumed that all grains have a constant electrostatic potential $\phi = 5$ V, and for different sizes this corresponds to different charges. For grains of radius larger than 1 μm, the Lorentz force is a minor factor in comparison to the other forces, and the qE term due to the solar wind electric field is small compared to the force due to the magnetic field. Consequently it is assumed that the electric field is negligibly small, such that $\boldsymbol{E} = 0$. For the magnetic field, a simple Parker Spiral model is used, and solar variability and magnetic field polarity flipping are not considered (Poppe, 2016).

In the fourth term, the first factor corresponds to the solar irradiance, where we assume a radiation pressure coefficient of $Q_{pr} = 1$. This term is dependent

on the size of the grain, a_d. Inside the square bracket, the first term 1 is the solar radiation pressure, and the second term is the solar wind particle pressure. The $\hat{\boldsymbol{r}}$ indicates that the forces are along the position vector of the dust grain. The very last term is the combined effect of Poynting-Robertson drag and solar wind drag, and is a force that works in the direction of the dust grain velocity. The w is a factor quantifying the influence of the solar wind drag, and is taken to be $w = 0.35$ (Poppe, 2016).

The mass loss processes that impact the water-ice grains are sublimation, solar wind sputtering, and for this work we have also included the effect of photo-sputtering, which was not previously incorporated in the model. These effects are dynamically taken into account when tracking the grains. For the silicate, the sublimation and photosputtering rates are set to be zero, and only solar wind sputtering will erode the silicate grains. Mass loss due to collisions between Kuiper belt grains, or collisions between interstellar- and Kuiper belt grains are not included in the model. If two dust particles collide they will be fragmented, and the fragments are significantly smaller than the size interval considered here. Additionally, the collisional lifetimes are sufficiently longer than the other mass loss processes (Poppe, 2023).

After the grains are launched, a Bulirsch-Stoer integrator is used to trace the dynamical evolution of the grains (Poppe, 2016). The simulation tracks individual grains until they either reach the inner Solar System, inside 0.1 AU, or have positive orbital energy and are ejected from the Solar System. However, if neither of these occur the simulation will terminate after one billion years. This is because the collision rate, while being lower than the other mass loss processes, is still sufficiently high so that within this time a collision would take place. In the model it is also assumed that the Kuiper belt remains stable during the lifetime of the grains, and that there are no major re-arrangements occurring.

We will be simulating grains that are pure silicates as well as grains that are launched with a silicate core and a water-ice mantle, at discrete grain sizes between 1 μm and 100 μm. The mass densities for the silicate is set to be $\rho_{sil} = 2$ g cm^{-3}, and the density for water-ice is $\rho_{ice} = 1$ g cm^{-3}. All the constants used in the simulations are summarised in Table A.1 in the appendix, and the model yields the output parameters described in Table 4.3.

Parameter	Description
t	Time along the dust grain trajectory integration [yrs]
t_{int}	The current integration time, determined dynamically by the code [yrs]
x	Dust grain Cartesian x position [AU]
y	Dust grain Cartesian y position [AU]
z	Dust grain Cartesian z position [AU]
v_x	Dust grain Cartesian x velocity [AU/yr]
v_y	Dust grain Cartesian y velocity [AU/yr]
v_z	Dust grain Cartesian z velocity [AU/yr]
r	Dust grain radius [m]

Table 4.3: Output parameters of the model used for simulating the dust grain trajectories.

4.4 Computing the orbital elements

After having performed simulations of dust grain trajectories, we want to compute the eccentricity and semi-major axis to describe the orbits of the grains. The eccentricity vector for a Kepler orbit, assuming a two-body problem, is given by

$$\boldsymbol{e} = \frac{\dot{\boldsymbol{r}}_s \times \boldsymbol{L}}{GM} - \frac{\boldsymbol{r}_s}{r_s} \tag{4.6}$$

where $\boldsymbol{L} = \boldsymbol{r}_s \times \dot{\boldsymbol{r}}_s$ is the angular momentum. This equation only takes into account the force of gravity, and is therefore only valid for Kepler orbits. Additional forces will cause the eccentricity to vary along an orbit, as these forces will perturb the grains, causing them to deviate from a perfect ellipse. One of the major perturbing forces that affect the dust grains is the radiation pressure force. This can be incorporated into equation 4.6 through the β-value in the following way:

$$\boldsymbol{e} = \frac{\dot{\boldsymbol{r}}_s \times \boldsymbol{L}}{GM(1-\beta)} - \frac{\boldsymbol{r}_s}{r_s} \tag{4.7}$$

Figure 4.11 shows the comparison between the effective eccentricity for a 10 μm core-mantle particle, calculated using equations 4.6 and 4.7. The blue curve represents the eccentricity taking into account only the force of gravity, and the orange curve is the eccentricity when including the β-value.

We can see that when we include the radiation pressure force in the equation, the oscillations present in the blue curve are significantly reduced. However, there are still some oscillations, and we can see these particularly close to zero years, two and four million years.

Because we are interested in the mean behaviour of the grains, we will compute the eccentricity using the following equation:

$$e = \frac{r_{aph} - r_{per}}{r_{aph} + r_{per}} \tag{4.8}$$

where r_{aph} is the aphelion of an orbit, and r_{per} is the perihelion. These values are found by iterating through the values of the heliocentric distance r_s, and finding the maximum and minimum distances from the Sun per orbit. The eccentricity calculated using this method is shown in the green curve in Figure 4.11. This yields the orbit averaged eccentricity, without any major oscillations. There are still some small-scale oscillations, which arises due to the fact that the position of the dust grains is only measured at discrete points, with a varying amount of years between each point. We initially employed equations 4.6 and 4.7 to calculate the eccentricity, as this was more computationally effective than calculating it using equation 4.8.

When we have the perihelion and aphelion of an orbit, we can also compute the semi-major axis by

$$a_{sma} = \frac{r_{aph} + r_{peri}}{2} \tag{4.9}$$

This is calculated and displayed in Figure 4.12, for the same dust grain as in Figure 4.11. The increase in eccentricity at approximately 2 million years is due to a capture of the mean-motion resonance with Neptune, and it stays in resonance for almost three million years, which is confirmed by a constant semi-major axis. At approximately 5 million years, the grain becomes gravitationally chaotic, before it is ejected from the Solar System.

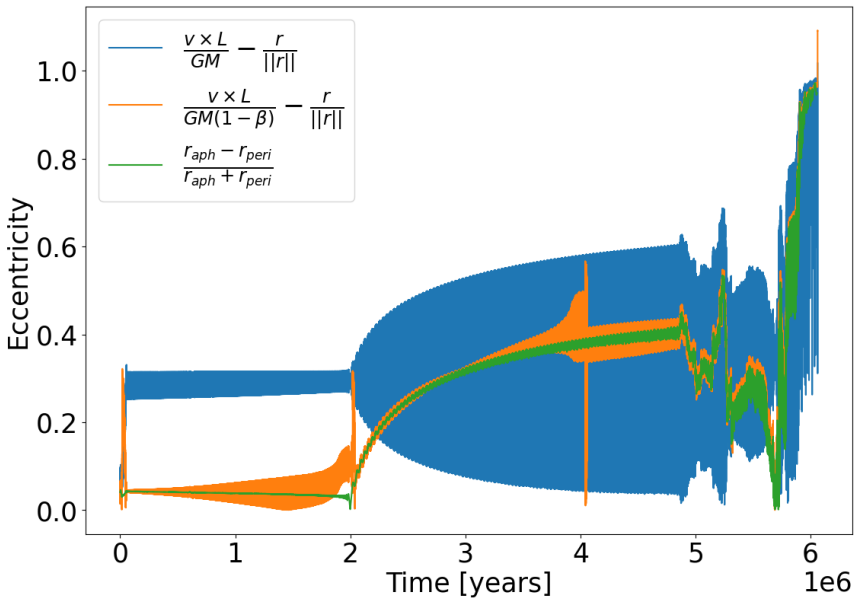

Figure 4.11: Comparison between the eccentricities computed using equations 4.6, 4.7 and 4.8, for a grain with total radius of 10 μm, and a silicate core of 1 μm.

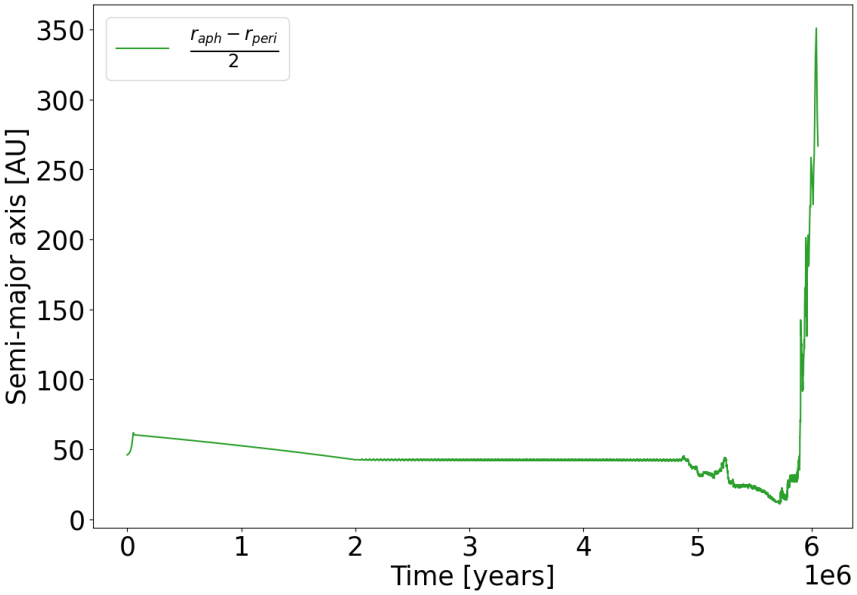

Figure 4.12: Semi-major axis computed using equation 4.9 for a 10 μm core-mantle grain.

5

Results and analysis

This chapter presents the results derived from the dust grain simulations conducted using the model described in Section 4.3. The aim of these simulations is to assess the variations in trajectory of the grains when assuming a mixed particle composition, in comparison to pure silicate grains. To begin with, we consider trajectories of individual grains, to investigate how the radius, heliocentric distance and orbital elements evolve throughout their lifetime. This is presented in Section 5.1. By studying the outcomes of these case studies, it becomes apparent how grains with different silicate and water-ice radii behave. This allows us to determine which silicate core and ice mantle sizes should be considered for the numerical experiment, which is presented in Section 5.2, where numerous grains are simulated. This chapter concludes by comparing the New Horizons SDC data to the simulation results in Section 5.3.

5.1 Case studies

In this section, we simulate and investigate the behaviour of grains with different silicate core and water-ice mantle sizes, assuming all the grains are launched with the same initial conditions in the Kuiper belt. Figures 5.1 and 5.2 show the heliocentric distance, radius, eccentricity, and semi-major axis for grains with a total radius $r_{tot} = 10$ μm and varying silicate core sizes of 1, 2, 3 and 4 μm. The plots show the first million years of the grains' lifetime, and we can see the impact on their trajectory as the water-ice mantle erodes.

For the grain with a 1 μm core in Figure 5.1a, the heliocentric distance, eccentricity and semi-major axis increase significantly as the water-ice mantle erodes. Immediately after the grain is launched from the parent object, the eccentricity is 0.100, and once the grain has eroded to a size of 1 μm, the eccentricity has increased to a value of 0.137. In the case of a 2 μm core, shown in Figure 5.1b, these parameters still exhibit an increase as the water-ice mantle erodes, but the effect is less pronounced. Initially the grain is launched with an eccentricity of 0.100, which increases to 0.120 after the ice has eroded.

As the ice to silicate ratio becomes even smaller, meaning the silicate core increases and the water-ice mantle decreases, displayed in Figures 5.2a and 5.2b, the influence of the water-ice mantle becomes less prominent. The grains start to behave more like pure silicate particles, as shown in Figure 5.3a. As the radius of the grain decreases from 10 μm to 3 or 4 μm, the heliocentric distance does not increase significantly, but remains closer to its initial position.

From these simulations, we can see that the presence of a water-ice mantle is significant, but only if the core size is sufficiently smaller than the water-ice mantle. For this reason, we choose to investigate grains that have 1 μm silicate core, and total radius of 1 μm, i.e. a pure silicate particle, 10 μm, and 100 μm. The heliocentric distance, radius, orbital eccentricity and semi-major axis for these three grain sizes are plotted in Figure 5.3. The first million years of the grains' lifetimes are shown. We note that these grains are launched with the same initial conditions, yet their initial eccentricities are noticeably different. The pure silicate grain, as seen in Figure 5.3a, is pushed onto a more elliptical orbit with eccentricity ~ 0.390 as soon as the grain is launched, which gradually decreases over time. The 10 μm grain, as discussed above, has an initial eccentricity of 0.100, and gets a higher eccentricity as the water-ice mantle erodes. The 100 μm grains has an initial eccentricity of ~ 0.088, which increases to ~ 0.125 when the ice has eroded.

From these simulations, it can be seen that there is a principle difference between a pure silicate grain and grains with a water-ice mantle. Grains that are launched as pure 1 μm silicates will immediately be pushed onto more elliptical orbits, as the radiation pressure force is more dominant than the force of gravity. The grains that have a water-ice mantle will however not be pushed onto highly elliptical orbits, because the grains are large enough that the radiation pressure force is not significant compared to the gravitational force. As the ice erodes, the eccentricity gradually increases, but remains relatively low in comparison to the pure silicate grain, even after reaching a size of 1 μm. During the time period when the ice erodes, the grain has time to stabilise its orbit, such that it remains closer to the orbit of the parent object, even after the ice has eroded. This has an implication on the distribution of the Kuiper belt grains, which will be apparent in the numerical experiment presented in Section 5.2.

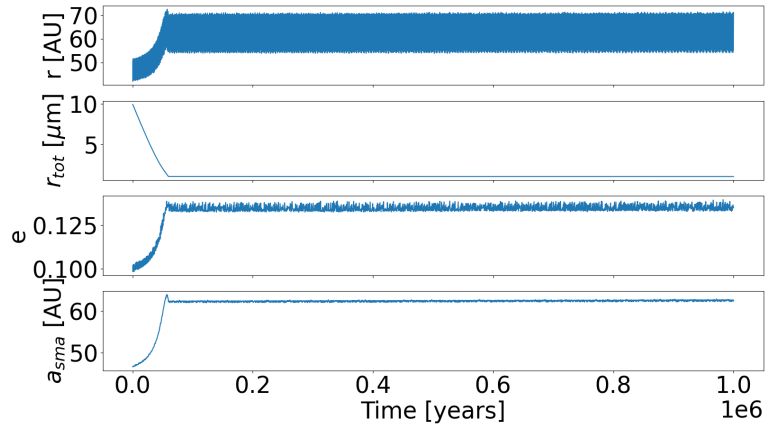

(a) $r_{tot} = 10$ μm, $r_{sil} = 1$ μm

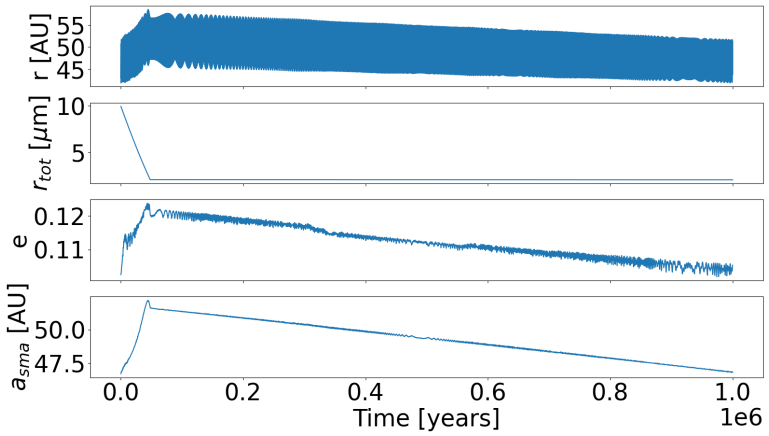

(b) $r_{tot} = 10$ μm, $r_{sil} = 2$ μm

Figure 5.1: The heliocentric distance r, radius r_{tot}, eccentricity e and semi-major axis a_{sma} as a function of time for grains with total radius $r_{tot} = 10$ μm, and silicate core of 1 and 2 μm.

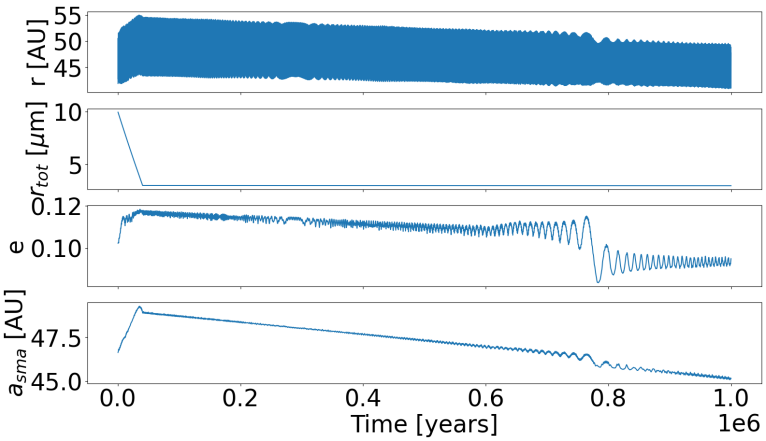

(a) $r_{tot} = 10$ μm, $r_{sil} = 3$ μm

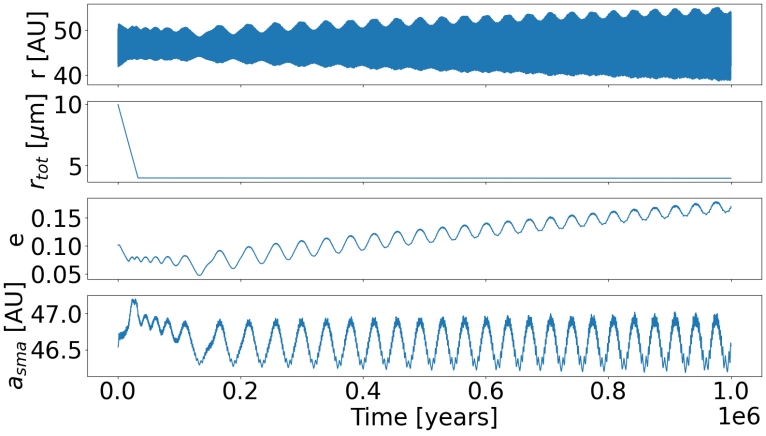

(b) $r_{tot} = 10$ μm, $r_{sil} = 4$ μm

Figure 5.2: Heliocentric distance, radius, eccentricity and semi-major axis as a function of time for grains with total radius $r_{tot} = 10$ μm, and silicate cores 3 and 4 μm.

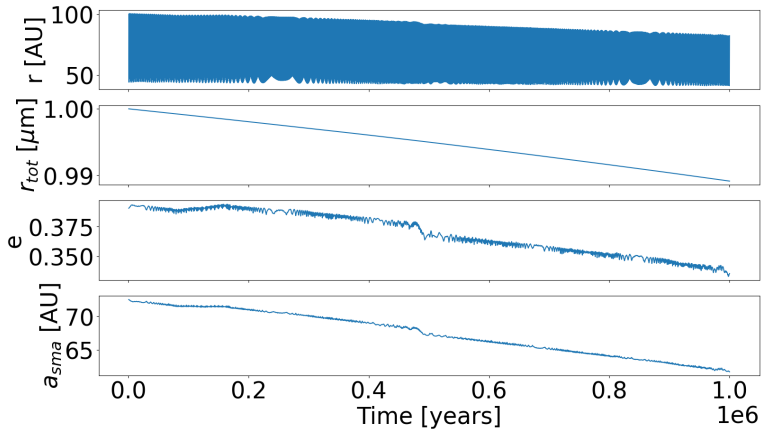

(a) $r_{tot} = 1$ μm, $r_{sil} = 1$ μm

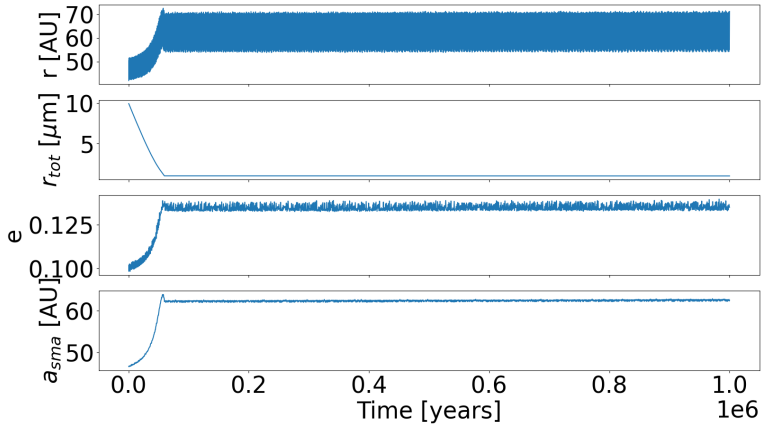

(b) $r_{tot} = 10$ μm, $r_{sil} = 1$ μm

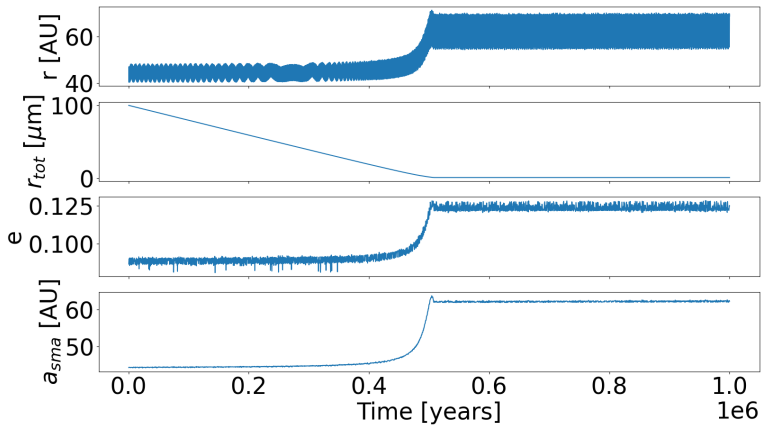

(c) $r_{tot} = 100$ μm, $r_{sil} = 1$ μm

Figure 5.3: Heliocentric distance, radius, eccentricity and semi-major axis for grains with a silicate core of $r_{sil} = 1$ μm, and total radii of 1, 10, and 100 μm.

5.2 Numerical experiment

In order to see the evolution of the dust grains in the Kuiper belt, we perform a numerical experiment by simulating 300 grains in total for the grain sizes presented in Figure 5.3, with 100 grains for each size. The aim is to get a distribution of the heliocentric distance, orbital eccentricity and semi-major axis of the grains. As described in Section 4.3, the grains are launched with random initial conditions in the dynamically cold region of the Kuiper belt, between 42.5 and 44.5 AU. The eccentricities are chosen randomly between 0 and 0.1, and the population of grains has inclinations of less than 10 degrees. We use a photosputtering rate of $\dot{s}_{ps} = 0.4$ μm yr^{-1} at 1 AU, as discussed in Section 4.2.

Each particle is simulated until it is ejected from the solar system or spiral into the sun, and if neither of these occur the simulation is terminated after one billion years. The entire lifetime of each grain will be traced and we follow the position vector and velocity vector for each grain. When discussing the dynamics of the grains, we will refer to two stages of the grain lifetime: the first stage is the part of the lifetime when a grain still has its water-ice mantle, and the second stage refers to the lifetime after the ice mantle has eroded and only the silicate core remains.

We start by investigating the distribution of the grains by projecting the orbits into the ecliptic plane, and compute a 2D histogram of the x- and y-positions of the grains. This result is shown in Figure 5.4, and the distribution is sufficient for illustrating the results, as the inclinations mainly stay within 3 degrees of the ecliptic plane. We can see that the 10 and 100 μm grains have a higher number density and are more concentrated within the Kuiper belt, compared to the 1 μm grains. Particularly, the 100 μm grains have the highest number density in the dynamically cold region of the Kuiper belt, where the grains originate. Furthermore, the 1 μm grains tend to have more elongated orbits and form a broader band in the Kuiper belt.

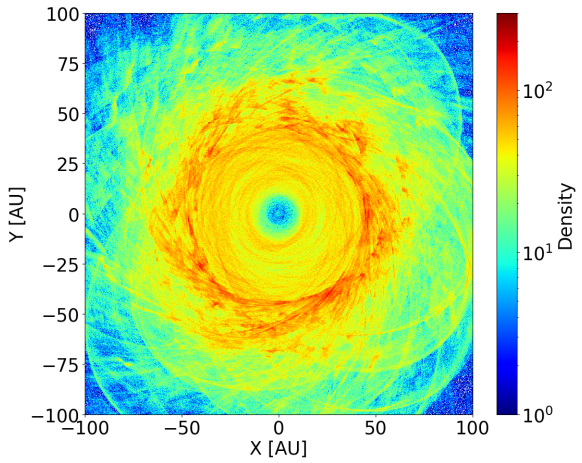

(a) 1 μm grains

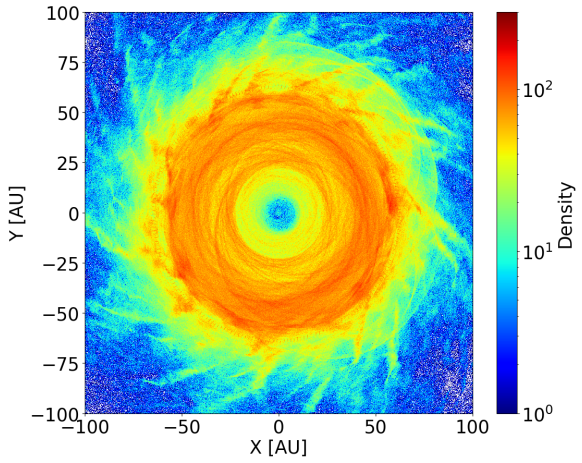

(b) 10 μm grains

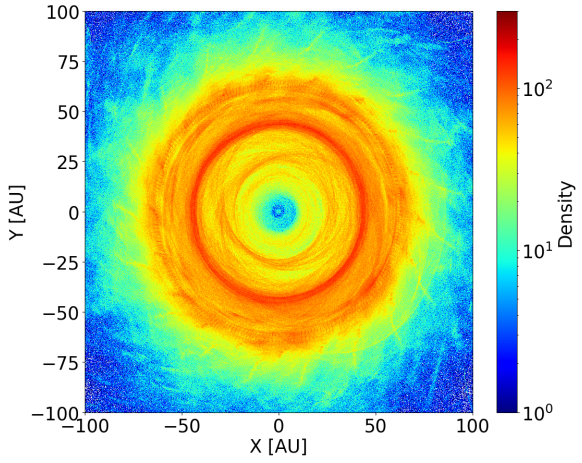

(c) 100 μm grains

Figure 5.4: 2D distributions of the x- and y-positions for particles with a 1 μm silicate core and a total radius of 1, 10 and 100 μm. 100 grains have been simulated for each size.

From the data set we derive the heliocentric distance for all 300 grains at each point along the orbit, and compute the eccentricity and semi-major axis per orbit, using equations 4.8 and 4.9, respectively. From these values, we compute the probability density for each parameter. Starting with the heliocentric distance, the values are divided into 1000 bins between 0 and 200 AU. The position vectors corresponding to each distance are allocated to their respective bins, which is then normalised to return a probability density such that the area under the curve integrates to 1.

In Figure 5.5 we have plotted the probability density of the heliocentric distance for the three different particle sizes, with each size having 100 simulated grains. The 100 μm particles have a peak at 43-44 AU, corresponding to the distance where the dust grains originate. There is also a second peak at approximately 63 AU. This is the distance that the grains reach after the water-ice mantle has eroded, as can be seen in Figure 5.3c. The 10 μm particle, in addition to having a peak density at 44 AU, has another peak at 57 AU. We also see that beyond the second peak, the probability density for both the 10 and 100 μm grains decreases, whereas the pure silicate grains have higher probability densities at longer distances. This is also apparent from the x- and y-distribution in Figure 5.4a.

To verify that the second peaks observed at 57 AU and 63 AU for the 10 and 100 μm grains, respectively, correspond to the heliocentric distance after the water-ice mantle has eroded, we compute the probability densities including only the second stage of the grains' lifetimes. This is shown in Figure 5.6. The lineplots represent the heliocentric distances for the entire lifetime of the grains, whereas the filled lineplots represent only the second stage of the lifetime of the grains. From the figure we can see the influence of the water-ice mantle on the grain trajectories. It is evident how the filled lineplots differ from the blue curve, despite these three curves representing the same grain size. When excluding the first stage of the lifetime for the 100 μm grains, the probability density at $\sim$ 44 AU becomes lower, and the peak at 63 AU remains. For the 10 μm grain, there is minimal difference between the two curves, indicating that the water-ice mantle erodes quickly. However, the mantle still has the effect of stabilising the orbit so the grains remain closer to the parent object, and preventing them from being pushed out to farther distances, as observed with the 1 μm grains.

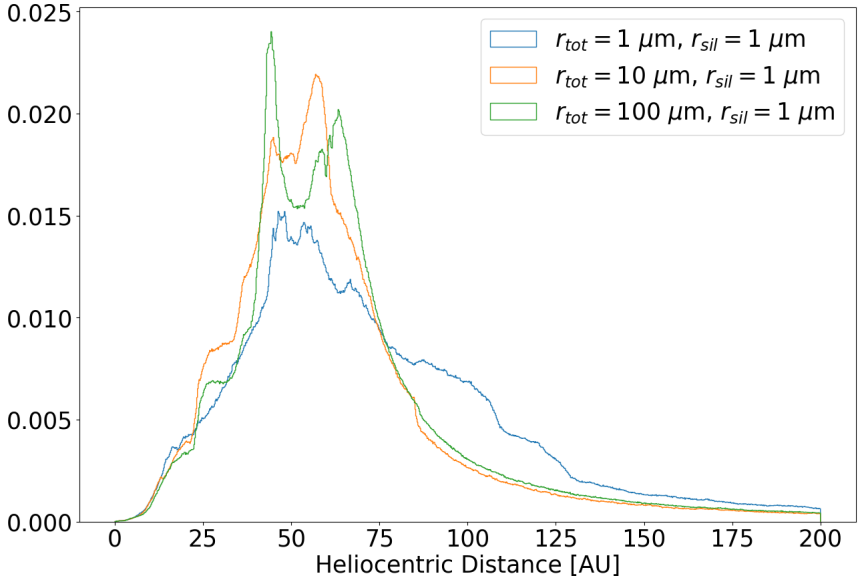

Figure 5.5: Probability density of the heliocentric distance for grains with a silicate core of 1 μm, and total radii of 1, 10 and 100 μm. 100 grains have been simulated for each size.

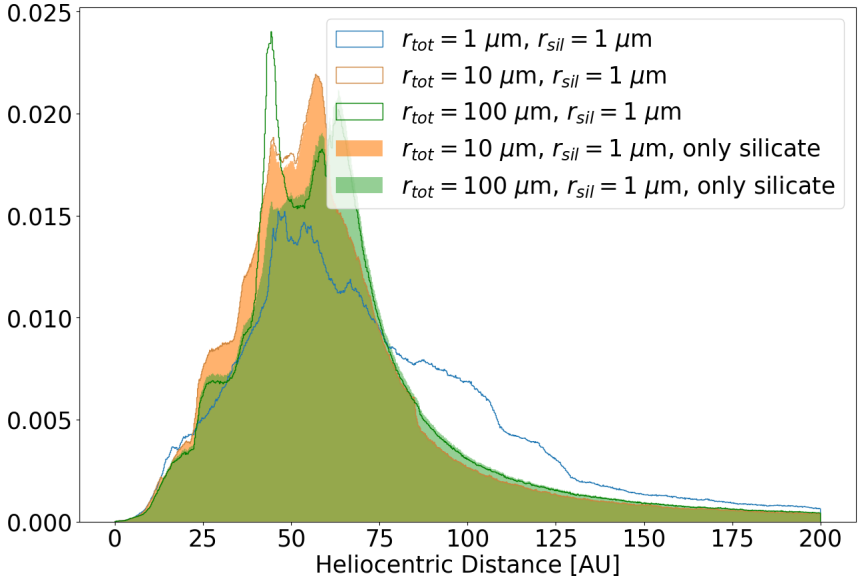

Figure 5.6: Probability density of the heliocentric distance for the three different grain sizes. The lineplots are the same as in Figure 5.5, and includes the values for the entire lifetime of the grains, and the filled lineplots only include the second stage of the lifetime of the grains.

Next we compute the probability density of the eccentricity, dividing the values into 1000 bins between 0 and 1 and normalising the histogram. These are shown in Figure 5.7 for the three grain sizes. The grains are launched with an eccentricity between 0 and 0.1, and for the 100 μm particles we can see how they mostly maintain low eccentricities for the majority of their lifetime, with values less than 0.2. The 10 μm grains also tend to remain at low eccentricities, mainly between 0 and 0.2, but they have slightly more elliptical orbits compared to the 100 μm grains. The reason for this is that the β-value is higher for smaller grains, leading to more elliptical orbits. In addition, it takes less time for the water-ice mantle to erode on the 10 μm grains, so they have a shorter timescale to stabilise their orbits, which is confirmed by the plots in Figure 5.3. For both the 10 and 100 μm grains, the probability is low for them having orbits with eccentricity above 0.5.

The 1 μm grains, i.e. the pure silicates, are also launched with eccentricities less than 0.1, but are rapidly pushed onto more elliptical orbits, due to their high β-value. These grains have a higher probability of having eccentricities around 0.4 to 0.5. There is still some probability for the grains to have eccentricities between 0 and 0.35, which can be due to the influence of solar wind drag and Poynting-Robertson drag. These forces cause the grains to lose orbital energy, and their impact is most significant for smaller grains.

The effect of the water-ice mantle is thus making the grains remain at low-eccentricity orbits, close to the orbital elements of the parent object. Even if the ice mantle erodes quickly, it will give the grains time to stabilise their orbits, whereas the pure silicate grains will immediately be pushed onto more elliptical orbits as soon as they are launched, because the β-value is high.

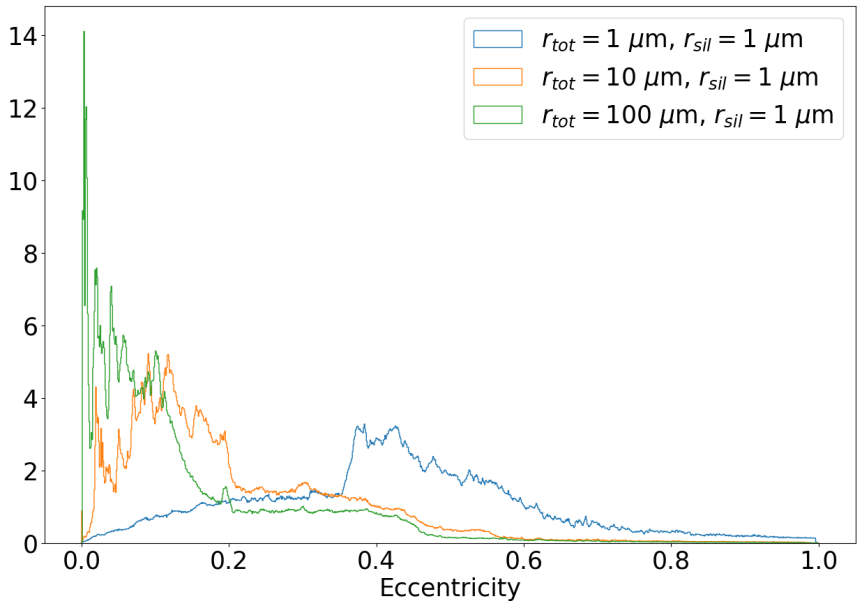

Figure 5.7: Probability density of the eccentricities for grains with a silicate core of 1 μm, and total radii of 1, 10 and 100 μm. 100 grains have been simulated for each size.

The probability density of the semi-major axis for the three grain sizes is shown in Figure 5.8, where the values are divided into 1000 bins between 0 and 100 AU, and normalised. We can see that the 10 and 100 μm grains have a peak density at $\sim$ 42 AU, which is just below the distance where the grains originate. At this semi-major axis, the grains are likely captured in a 3:5 mean-motion resonance with Neptune (Lykawka and Mukai, 2007). We note that at this distance, there is a dip in the probability density of the pure silicate grains. A possible explanation is that the radiation pressure exerted on the grains causes them to be pushed outwards as soon as they are launched, as discussed above.

At approximately 35 AU, the 10 and 100 μm grains have another peak in the distribution, whereas there is a depletion of 1 μm grains. This semi-major axis corresponds to a 4:5 resonance with Neptune (Lykawka and Mukai, 2007), suggesting that the grains are captured in this resonance. The grains can be decelerated and spiral inwards within the Solar System by solar wind drag and Poynting-Robertson drag. The drag effects are more significant for smaller grains, and could explain why there is a higher probability density of 10 μm grains in the 4:5 resonance with Neptune, compared to the 100 μm grains. It is interesting to note that there is an absence of 1 μm grains at this distance. The increase in the probability density at $\sim$ 60 AU for the water-ice grains is

likely due to the grains being captured in 1:3 resonance with Neptune, which corresponds to a semi-major axis of approximately 62 AU (Lykawka and Mukai, 2007).

At a distance of 13 AU, the silicate grains have a distinct peak in the semi-major axis density. This innermost peak is possibly related to resonance with Saturn. In addition, there is a depletion of grains with semi-major axes less than 13 AU. This can be due to the dust grains experiencing close encounters with Saturn or Jupiter, which can transfer sufficient energy for the dust grains to be ejected from the Solar System. Resonance with Saturn is generally less stable than resonance with Neptune, and the longer the grains remain captured in the resonance, the higher is the probability of the larger grains being ejected. The pure silicate grains have multiple smaller peaks, which correspond to individual resonances with Neptune. The perturbative forces will push smaller grains out of resonance faster than the larger grains. Consequently, since the resonances experienced by the 1 μm grains are relatively weak, they tend to average out.

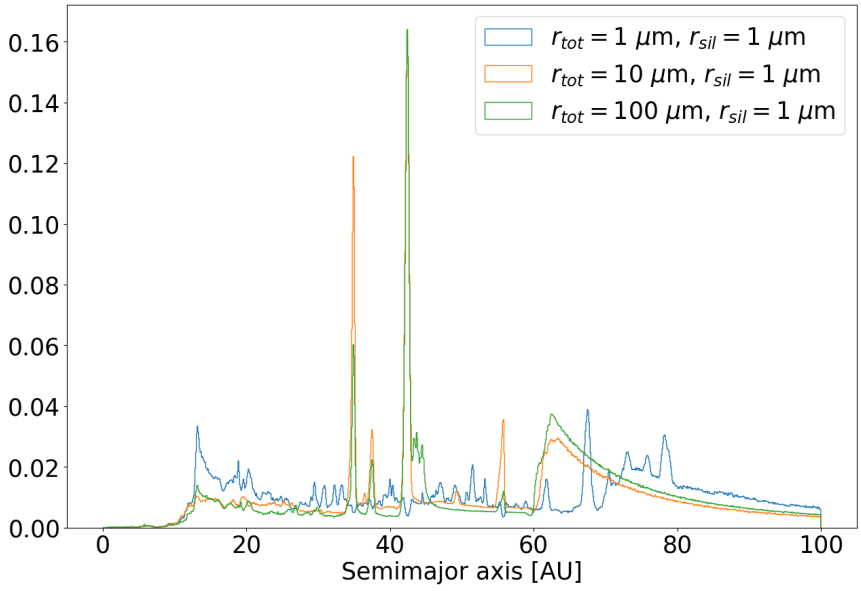

Figure 5.8: Probability density of the semi-major axis for grains with a silicate core of 1 μm, and total radii of 1, 10 and 100 μm. 100 grains have been simulated for each size.

So far we have conducted a numerical experiment of grains with a 1 μm core. However, we also simulate and investigate the behaviour of grains with a 0.7 μm core, in order to assess how the results depend on the size of the silicate core. The probability density of the heliocentric distance for grains with a 0.7

μm core, and total radii of 0.7, 10 and 100 μm are shown in Figure 5.9, with 100 grains simulated for each size. Comparing these results to those presented in Figure 5.5, we can see that the high probability density at $\sim$ 57 and $\sim$ 63 AU for the 10 and 100 μm grains with a 1 μm silicate core are less prominent for the grains with a 0.7 μm core. This suggests that the first stage of the grains' lifetimes, where they still retain their water-ice mantle, makes up a larger fraction of the overall lifetime for the 0.7 μm grains. Since the core size is smaller, a larger fraction of these grains is composed of water-ice. It is worth noting that even decreasing the size of the silicate core by 0.3 μm and replacing this with water-ice, leads to the 100 μm grains having a significantly higher probability density at the origin distance of $\sim$ 43 AU. In addition, we see that the 0.7 μm pure silicate grains have a higher probability density at larger distances in comparison to the 1 μm silicate grains.

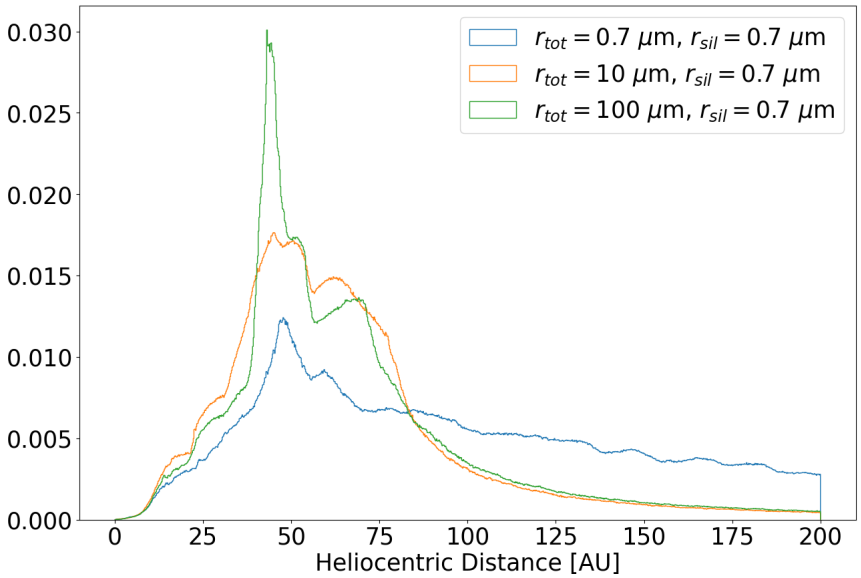

Figure 5.9: Probability density of the heliocentric distance for grains with a silicate core of $r_{sil} = 0.7$ μm, and total radii 0.7, 10 and 100 μm.

As discussed in Section 4.1, the initial assumption was that water-ice grains would have orbits that extended further out in the Solar System compared to the pure silicate grains, since the β-value for water-ice grains is higher than for asteroidal grains. However, from the simulations conducted using the model described in Section 4.3, we see that the silicate grains have more elliptical orbits in comparison to the grains with a water-ice mantle. The reason for this is that the 1 μm silicate grains will experience an immediate outward push due to the radiation pressure force as soon as they are launched. In contrast, grains with a water-ice mantle are large enough to not experience the immediate

outward kick exerted by radiation pressure. As the water-ice mantle erodes, the radiation pressure force gradually increases. This will give the grains time to stabilise their orbits and remain closer to the orbit of the parent object. However, we note that once the water-ice mantle has eroded, the heliocentric distance of the grains has increased from $\sim$ 43 AU to $\sim$ 57 – 63 AU, depending on the ice mantle sizes. These distances are beyond the boundary of the Kuiper belt, which is considered to extend only up to 50 AU. The results show that if we have larger dust grains that decrease in size, the resulting distribution of dust differs significantly from the distribution for the initially small grains.

5.2.1 Influence of the photosputtering rate

For the simulations presented above, a photosputtering rate of $\dot{s}_{ps} = 0.4$ μm yr^{-1} at a distance of 1 AU from the Sun was used. To investigate the influence of this rate on the result, we also run simulations of the same grain sizes as before, i.e. $r_{sil} = 1$ μm and $r_{tot} = 1$, 10 and 100 μm, with a 10 times lower photosputtering rate, $\dot{s}_{new} = 0.04$ μm yr^{-1}. In Figure 5.10 we have compared the probability densities of the heliocentric distance for the original photosputtering rate, and the slower rate. It can clearly be seen that the 100 μm grain with the slower rate remains at a distance of $\sim$ 43 AU for longer, as it takes significantly more time for the water-ice mantle to erode. However, for the 10 μm grains, reducing the photosputtering rate has the effect of shifting the distribution out to larger distances. Thus it is evident that photosputtering is significant on the behaviour of mixed composition grains in the Kuiper belt.

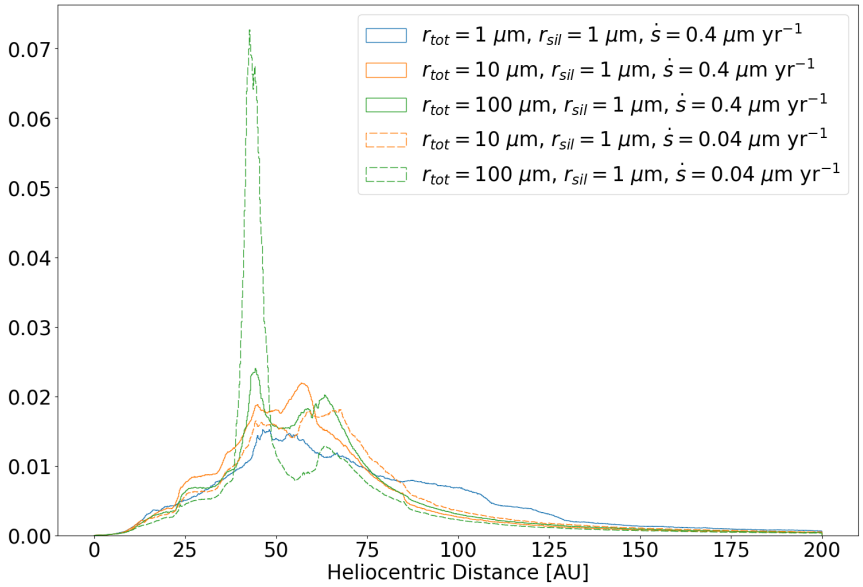

Figure 5.10: Probability density of the heliocentric distance for the three grain sizes, comparing a photosputtering rate of $\dot{s}_{ps} = 0.4\ \mu$m yr^{-1} and $\dot{s}_{new} = 0.04\ \mu$m yr^{-1}.

5.3 Connection to observational data

In the presented results, only a limited number of trajectory calculations were made. Additionally, there is limited available data of the dust flux in the Kuiper belt. Despite these limitations, it is possible to establish a connection between the simulations discussed above and the measurements made by New Horizons SDC. Figure 3.1 is taken from Bernardoni et al. (2022) and shows the dust flux onto the SDC. From the data points we can see that there is an increase in dust impacts between 40 and 50 AU, and that the measured flux is higher than predicted by the model. From the probability density of the heliocentric distance, shown in Figure 5.6, it is evident that the dust probability increases significantly at $\sim$ 42 AU, and remains high until it decreases beyond 63 AU. Since the SDC is sensitive to dust grains with sizes between 0.5 and 5 μm, we only consider the filled lineplots for this comparison, since these grains have sizes of 1 μm or smaller.

If a 100 μm grain, consisting of a silicate core of 1 μm and outer water-ice mantle, is a good representation of dust in the Kuiper belt, it is expected that the dust ring will extend to distances farther than 50 AU, and start to decrease beyond 63 AU. However, if the grains are launched with a size of 1 μm from a parent object, we expect the dust cloud to extend even further out in the Solar

System. Thus, the presence of water-ice grains in the Kuiper belt could possibly explain the dust flux observed with SDC, as the simulations show that these grains have a high probability density around 50 AU and beyond. For future measurements conducted with SDC, we expect that at approximately 65 AU there would be a disappearance of the water-ice, but it would keep measuring impacts from pure silicate grains further out in the Solar System.

6

Conclusion

This master's thesis aimed to investigate the behaviour of dust grains in the Kuiper belt and explain the difference observed between the measured dust flux and the predicted flux. A central part of this investigation has been to examine the difference in behaviour between silicate grains, and grains that have a water-ice component.

The β-value has been compared for silicate and water-ice grains, and we performed orbit calculations of grains with these compositions, taking into account only the force of gravity and radiation pressure force. This showed that water-ice grains have a higher β-value, meaning they are pushed further out in the Solar System by radiation pressure, in comparison to silicate grains.

A significant part of this thesis was the calculation of the photosputtering rate on water-ice grains in the Solar System, which was derived for the first time in this thesis. The derivation was based on calculations made by Grigorieva et al. (2007) of the photosputtering rate for other star systems. We used the absorption coefficient for water-ice provided by Li (2023), which was different from the one used by Grigorieva et al. (2007), and that we found to be more realistic. It became evident that for water-ice grains, the erosion due to photosputtering is higher by two orders of magnitude than the erosion due to solar wind sputtering. This indicates that the mass loss due to photosputtering is significant for water-ice, and that it influences the trajectory of a dust grain.

A model developed by Poppe (2016), that was implemented at University of Cal-

ifornia, Berkeley, was used to simulate dust grains originating in the Kuiper belt. The model has previously incorporated the mass loss due to sublimation and solar wind sputtering on silicate grains. For this thesis, the model was adapted to include a water-ice component, by assuming a core-mantle composition, as well as implementing the mass loss due to photosputtering.

By simulating pure silicate grains, and grains with a water-ice mantle, it was observed that the core-mantle grains exhibited significantly different behaviour compared to the pure silicate grains. The pure silicate grains with a radius of 1 μm were immediately pushed onto more elliptical orbits, while the core-mantle grains experienced a gradual increase in radiation pressure as the water-ice mantle eroded, and thus a gradual increase in eccentricity.

We conducted a numerical experiment simulating the trajectories of 300 grains. Each grain had a silicate core of size $r_{sil} = 1$ μm, and 100 grains was simulated for each of the sizes $r_{tot} = 1, 10$ and 100 μm. The probability density of heliocentric distance, eccentricity, and semi-major axis was derived for the three grain sizes. The results show that pure silicate grains have more elliptical orbits and are pushed further out in the Solar System compared to grains with a water-ice mantle. The water-ice mantle has the effect of stabilising the grains, keeping them closer to the position of the parent object, even after the ice mantle has eroded. We found that the core-mantle particles form a stable dust ring in the Kuiper belt, due to the water-ice component. For all cases considered, the grains extend beyond 50 AU, but the small silicate grains go further out in the Solar System than the grains with a water-ice mantle.

The simulations were also compared to the New Horizons SDC measurements, which were the motivation for the thesis. The SDC measurements show a higher flux than predicted around 50 AU, which is the outer edge of the Kuiper belt. The simulations indicated that water-ice grains originating in the dynamically cold Kuiper belt have a high probability density between approximately 42 AU and 65 AU. This suggests that the presence of water-ice grains could potentially explain the dust flux observed with SDC, and implies that the flux should decrease beyond approximately 63 AU. However, the pure silicate grains have orbits that extend further out in the Solar System, meaning the SDC would observe Kuiper belt dust far beyond 50 AU.

Bibliography

S. Andersson, A. Al-Halabi, G.-J. Kroes, and E. F. van Dishoeck. Molecular-dynamics study of photodissociation of water in crystalline and amorphous ices. *J. Chem. Phys.*, 124(6):064715–064715, 2006. doi: 10.1063/1.2162901.

P. Artymowicz. Radiation pressure forces on particles in the beta pictoris system. *The Astrophysical Journal*, 335:L79–L82, 1988. doi: 10.1086/185344.

C. Baumann, M. Myrvang, and I. Mann. Dust sputtering within the inner heliosphere: a modelling study. *Annales Geophysicae*, 38(4):919–930, 2020. doi: 10.5194/angeo-38-919-2020.

E. Bernardoni, M. Horányi, A. Doner, M. Piquette, J. R. Szalay, A. R. Poppe, D. James, S. Hunziker, V. Sterken, P. Strub, C. Olkin, K. N. Singer, J. Spencer, A. Stern, and H. Weaver. Student dust counter status report: The first 50 au. *The Planetary Science Journal*, 3(3):69, 2022. doi: 10.3847/PSJ/ac5ab7.

J. A. Burns, P. L. Lamy, and S. Soter. Radiation forces on small particles in the solar system. *Icarus*, 40(1):1–48, 1979. doi: 10.1016/0019-1035(79)90050-2.

O. Coddington, J. L. Lean, D. Lindholm, P. Pilewskie, M. Snow, and N. C. P. (2017). Noaa climate data record (cdr) of solar spectral irradiance (ssi). `https://www.ncei.noaa.gov/products/climate-data-records/solar-spectral-irradiance`, 2023. Accessed: 06.03.2023.

R. I. Dawson and R. Murray-Clay. Neptune's wild days: Constraints from the eccentricity distribution of the classical kuiper belt. *The Astrophysical Journal*, 750(1):43, 2012. doi: 10.1088/0004-637X/750/1/43.

P. Fortescue, G. Swinerd, and J. Stark. *Spacecraft Systems Engineering*. John Wiley & Sons, 4 edition, 2011.

A. Grigorieva, P. Thébault, P. Artymowicz, and A. Brandeker. Survival of icy grains in debris discs - the role of photosputtering. *Astronomy & Astrophysics*, 475(2):755–764, 2007. doi: 10.1051/0004-6361:20077686.

A. Li. Personal communication, March 2023.

P. S. Lykawka and T. Mukai. Dynamical classification of trans-neptunian objects: Probing their origin, evolution, and interrelation. *Icarus*, 189(1):213–232, 2007. doi: 10.1016/j.icarus.2007.01.001.

I. Mann. Interstellar dust in the solar system. *Annual Review of Astronomy and Astrophysics*, 48(1):173–203, 2010. doi: 10.1146/annurev-astro-081309-130846.

T. Minato, Köhler, M., Kimura, H., Mann, I., and Yamamoto, T. Momentum transfer to interplanetary dust from the solar wind. *Astronomy & Astrophysics*, 424(2):L13–L16, 2004. doi: 10.1051/0004-6361:200400037.

T. Mukai and G. Schwehm. Interaction of grains with the solar energetic particles. *Astronomy & Astrophysics*, 95(2):373–382, 1981.

M. J. Pecaut and E. E. Mamajek. Intrinsic Colors, Temperatures, and Bolometric Corrections of Pre-main-sequence Stars. *The Astrophysical Journal Supplement Series*, 208(1):9, 2013. doi: 10.1088/0067-0049/208/1/9.

A. Poppe. Personal communication, March 2023.

A. R. Poppe. An improved model for interplanetary dust fluxes in the outer solar system. *Icarus*, 264:369–386, 2016. doi: 10.1016/j.icarus.2015.10.001.

M. S. Westley, R. A. Baragiola, R. E. Johnson, and G. A. Baratta. Ultraviolet photodesorption from water ice. *Planetary and Space Science*, 43(10):1311–1315, 1995. doi: 10.1016/0032-0633(95)00088-M.

M. Wilck and I. Mann. Radiation pressure forces on “typical” interplanetary dust grains. *Planetary and Space Science*, 44(5):493–499, 1996. doi: 10.1016/0032-0633(95)00151-4.

A

Constants used in the model

Constants used in the model described in Section 4.3.

Parameter	Value	Description
Q_{pr}	1	Radiation pressure coefficient
w	0.35	Ratio between solar wind drag and Poynting-Robertson drag
ϕ	5 V	Electrostatic potential
ρ_{sil}	2 g cm^{-3}	Silicate density
ρ_{ice}	1 g cm^{-3}	Water-ice density
η	1	Fraction of dust surface covered in ice
m_{H_2O}	3×10^{-23} g	Water molecule mass
$Y_{p,wi}$	1.58	Proton yield for water-ice
$Y_{p,sil}$	7.22×10^{-3}	Proton yield for silicate
$Y_{\alpha,wi}$	6.84×10^{-2}	Alpha yield for water-ice
$Y_{\alpha,sil}$	0.587	Alpha yield for silicate
$\dot{s}_{ps}$	0.4 μm yr^{-1}	Photosputtering rate at 1 AU

Table A.1: The constants used in the model for simulating the dust grain trajectories.

B

Additional results

Radius (μm)	$\dot{s}_{ps,min}$ (μm yr^{-1})	$\dot{s}_{ps,max}$ (μm yr^{-1})
0.001	0.00316522	0.00407101
0.003	0.00951463	0.01223744
0.005	0.01588322	0.02042039
0.007	0.02221497	0.02852936
0.01	0.03143848	0.04022959
0.03	0.08208612	0.09976961
0.05	0.12511939	0.14624115
0.07	0.16822441	0.19151973
0.1	0.21999322	0.24542035
0.2	0.34400838	0.37401862
0.3	0.4144889	0.44695394
0.4	0.45296899	0.48665386
0.5	0.47198971	0.50616022
0.6	0.47933388	0.51356959
0.7	0.48014507	0.51423076
0.8	0.47770175	0.51154475
1	0.46973081	0.50304554
2	0.44420788	0.47605174
3	0.43320614	0.46444366
5	0.42361056	0.45432041
7	0.41917796	0.44964491
10	0.41566227	0.44593662
20	0.41114751	0.44112704
30	0.40954645	0.43945072
50	0.40615518	0.43591388

Table B.1: Photosputtering rate for water-ice grains at solar minimum and maximum at 1 AU from the Sun.

C Code

This appendix provides the scripts written in Python 3.10.4 used to perform the calculations in this thesis. Listing C.1 is used to compute the photosputtering rate for water-ice grains in the Solar System, using equations 2.8 and 2.7, with data from Li (2023). Listing C.2 is the script used to investigate the influence of β-value, and to solve Kepler's equation and compute the orbits of water-ice grains and asteroidal grains. Listing C.3 provides the code used to read the output from the simulations made at UC Berkeley, and compute the probability densities of the heliocentric distance, eccentricity and semi-major axis.

```
import numpy as np
import matplotlib.pyplot as plt
from scipy.interpolate import interp1d
from scipy import integrate
import netCDF4

AU = 1.496e+11 #m
h = 6.62607015e-34 #Plancks constant
c = 3e8      #m/s
kB = 1.381e-23 #Boltzmanns constant, m^2 kg s^-2 K^-1
radius_sun = 6.96e8 #m

def blackbody_spectrum(wavelength, temp):
    """
    Returns the blackbody spectrum in the given wavelength
     interval, depending on the temperature.
```

```
    """
    return 2 * np.pi * h * c**2/wavelength**5 * 1/(np.exp(h * c
    /(wavelength * kB * temp)) - 1) *1e-9 * radius_sun**2/AU**2
     #W/m^2 /nm

#temperature of the sun, and G0V and G2V type stars:
temp_sun = 5778 #K
temp_G0V = 5920 #K
temp_G2V = temp_sun

#getting the solar spectrum data:
#from https://www.ncei.noaa.gov/products/climate-data-records/
    solar-spectral-irradiance
ds = netCDF4.Dataset('ssi_v02r01_yearly_s1610_e2022_c20230120.
    nc')


#the solar spectral irradiance (SSI) at 1 AU:
ssi = ds['SSI'][:]   #at 1 AU

#defining the wavelength:
wl = ds['wavelength'][:] #nm
wl = np.array(wl)
time = ds['time'][:]


#computing the blackbody spectra for different temperatures:
bb_spectrum_sun = blackbody_spectrum(wl*1e-9, temp_sun)
bb_spectrum_G0V = blackbody_spectrum(wl*1e-9, temp_G0V)
bb_spectrum_G2V = blackbody_spectrum(wl*1e-9, temp_G2V)


#solar spectrum at solar minimum and maximum:
ssi_minimum = ssi[1954-1610, :]
ssi_maximum = ssi[1958-1610, :]


class Readfile():
    """Class that opens the file and reads each line."""
    def __init__(self, filename, number):
        f = open(filename, 'r')
        self.lines = f.readlines()
        del self.lines[:number]

    def info(self, column):
        """Function that divides the data into columns, converts
    the strings into float values and returns a variable for
    the given column."""
        variable_s = [line.split()[column] for line in self.lines
    ]
        variable = [float(num) for num in variable_s]

        return np.array(variable)

```

```
63 def qabs(filename):
64
65     qabs_file = Readfile(filename, 0)
66     wavelength = qabs_file.info(1)    #um
67     Qabs = qabs_file.info(2)
68
69     return Qabs, wavelength
70
71 qabs, wavelength= qabs('Qabs\\qabs_ice.dat')
72
73
74 #wavelength and qabs from Grigorieva et al. (2007), extracted
       from Figure 1 in the paper:
75 x = np.array([0.0851544221306799, 0.09328056095490911,
       0.10391229280446541, 0.11547847445094862,
       0.12649840814709193, 0.14227467119192555,
       0.15925266369564628, 0.16788184005837548,
       0.17113436358549103, 0.17403194747105277,
       0.1769786245639738, 0.1795440028888466,
       0.18214656743304922, 0.18478685722620336,
       0.18612133670103556, 0.1883668966183199,
       0.1943329780655824, 0.20486299685401005,
       0.21962024537249386, 0.2360059169505661,
       0.25667397132808817, 0.2731905027564194,
       0.28730351855951286, 0.302871242829912,
       0.32236048973350157, 0.3522768317600036, 0.364307131802286,
        0.3776529945293647, 0.4117120134410046,
       0.45100105940041146, 0.48698032718985673,
       0.5220599140058217, 0.5610103408231091,
       0.5928290412321082])
76 y = np.array([0.8856900537372823, 0.8592155864104907,
       0.9129797336536082, 0.9129797336536082, 0.9129797336536082,
        0.9129797336536082, 0.8856900537372823,
       0.4827145107195688, 0.1349421988949379,
       0.04390399802582445, 0.011205297461168651,
       0.002532937521652161, 0.0006464631846050354,
       0.00017531632528358106, 0.00007495394243391776,
       0.00003108756671638919, 0.00001971933044610369 3,
       0.00001546880288722048, 0.00001250830909667764,
       0.00000981212665398405, 0.00000724381647409 2314,
       0.00000724381647409 2314, 0.00000585746008 6482049,
       0.00000406963439 2538054, 0.00000329077583 58636903,
       0.00000235679722 3358971, 0.00000309698827 03321108,
       0.00000184878648 86148721, 0.00000136486925 77638086,
       8.657599505887908e-7, 7.904217466119893e-7,
       0.00000103866312 81226044, 0.00000140692329 80173346,
       0.00000202499690 83189904])
77
78
79 #the min and max energies used by grigorieva:
80 wavelengths_new = np.linspace(0.091*1e3, 0.24*1e3, 10000)
81
82
83 def interpolate(x_old, y_old, x_new):
```

```
84      f = interp1d(x_old, y_old, fill_value="extrapolate", kind="
        quadratic")
85      y_new = f(x_new)
86      return y_new
87
88  Qabs_Li = interpolate(wavelength*1e3, qabs, wavelengths_new)
89
90  Qabs_Grigorieva = interpolate(x*1e3, y, wavelengths_new)
91
92
93  flux_new = interpolate(wl, ssi[0, :], wavelengths_new)
94  bbspectrum_sun_new = interpolate(wl, bb_spectrum_sun,
        wavelengths_new)
95  bbspectrum_G0V_new = interpolate(wl, bb_spectrum_G0V,
        wavelengths_new)
96  bbspectrum_G2V_new = interpolate(wl, bb_spectrum_G2V,
        wavelengths_new)
97
98  ssi_min_new = interpolate(wl, ssi_minimum, wavelengths_new)
99  ssi_max_new = interpolate(wl, ssi_maximum, wavelengths_new)
100
101
102 def photosputtering_rate(F, Q_abs, wavelength):
103     """
104     Calculates and returns the photosputtering rate, using
        equations from Grigorieva et al. (2007).
105
106     F(wavelength, R) - incident stellar flux at position R of
        the grain, W * m^-2 * nm^-1
107     Q_abs(wavelength) - absorption coefficient
108     wavelength - nm
109     """
110
111     eta = 1      #fraction of surface covered in ice
112     m_h2o = 3e-23 * 1e-3     #mass of water-molecule, kg
113     Y = 1e-3        #photosputtering yield
114     rho = 917       #density of water ice, kg/m^3
115
116     N_abs = integrate.trapezoid(F * Q_abs * wavelength/(h * c),
        wavelength)     #number of absorbed photons, nm *s^-1 * m^-3
117     rate =  eta *m_h2o * Y * N_abs/(4 * rho)  #nm/s
118
119     return rate*1e-3/3.17098e-8 # um/yr
120
121
122 def get_rates(flux):
123     """
124     retriving the photosputtering rate for the given stellar
        flux
125     """
126
127     sputtering_rates = photosputtering_rate(flux, Qabs_Li,
        wavelengths_new)
128
```

```
    radius = np.array([0.001, 0.003, 0.005, 0.007, 0.01, 0.03,
     0.05, 0.07, 0.1, 0.2, 0.3, 0.4, 0.5, 0.6, 0.7, 0.8, 1, 2,
     3, 5, 7, 10, 20, 30, 50])*1e-6

    radius_rates = np.geomspace(radius[0], radius[-1], 10000)
    sputteringrates = interpolate(radius, sputtering_rates,
     radius_rates)

    return radius_rates, sputteringrates

radius_solarmin, sputteringrate_solarmin = get_rates(
    ssi_min_new)
radius_solarmax, sputteringrate_solarmax = get_rates(
    ssi_max_new)
```

Listing C.1: Code used to calculate the photosputtering rate as a function of radius

```
import numpy as np
import matplotlib.pyplot as plt
from scipy.interpolate import interp1d
from scipy import optimize


AU = 1.496e+11              #AU to meter
G = 6.67408e-11             #gravitational constant, m^3 kg^-1 s
    ^-2
mass_sun = 1.989e30         #kg
mu = G * mass_sun

eccentricity_parent = 0
semimajoraxis_parent = 40 * AU


def tau(a, beta):
    """
    Computes and returns the orbital period.

    a: semi-major axis
    """

    n = np.sqrt(mu * (1-beta)/a**3)  #mean motion
    tau = 2 * np.pi/n        #period of the orbit
    return tau


def g(E, M, e):
    """
    Kepler's equation for elliptical orbits. Used to find the
     eccentric anomaly, E.

    E: eccentric anomaly, which we want to solve for
    M: mean anomaly
    """

```

```
36      return E - e * np.sin(E) - M
37
38
39  def Kepler_elliptical(t, a, e, beta):
40      """
41      Solves Keplers equation. This is only valid for orbits with
         eccentricity between 0 and 1.
42
43      t: Time array of the orbit
44      a: semi-major axis of the orbit
45      e: eccentricity of the orbit
46      """
47
48      #calculate the mean motion:
49      n = np.sqrt(mu * (1 - beta) /a**3)
50
51      M = np.zeros(len(t))
52      E = np.zeros(len(t))
53      r = np.zeros(len(t))
54      theta = np.zeros(len(t))
55      rx = np.zeros(len(t))
56      ry = np.zeros(len(t))
57
58      E0 = 0.5
59      #iterating through the time array and solving Keplers
         equation and computing the position of the grain along the
         orbit:
60      for i in range(len(t)):
61          M[i] = n * t[i]                                    #mean
         anomaly
62          E[i] = optimize.fsolve(g, x0 = E0, args=(M[i], e))
         #Eccentric anomaly
63          r[i] = a * (1 - e * np.cos(E[i]))                    #
         heliocentric distance
64          theta[i] = 2 * np.arctan(np.tan(E[i]/2) * np.sqrt((1 + e)
          / (1- e)) )   #Theta as function of the eccentric anomaly,
          i.e. angle between Sun and the position of the grain
65
66          E0 = E[i]
67
68          #x and y positions:
69          rx[i] = r[i] * np.cos(theta[i])
70          ry[i] = r[i] * np.sin(theta[i])
71
72      return r, rx, ry
73
74
75  def velocity(semimajor_axis, r, beta):
76      """
77      Solves the vis-viva equation and returns the velocity.
78
79      r: array of the position of the dust along the orbit
80      """
81
```

```
82      return np.sqrt(mu * (1 - beta) * (2/r - 1/semimajor_axis))
83
84
85  def orbital_elements(beta, v, r):
86      """
87      Calculates and returns the semi-major axis, eccentricity and
          aphelion of an orbit
88
89      v: heliocentric speed
90      r: heliocentric radial distance
91      a: semi major axis
92      beta: ratio
93      """
94
95      semimajor_axis = 1/(2/r - v**2/(mu * (1 - beta)))  #[m]
96
97      e_dust = np.abs(1 - r/semimajor_axis)  #eccentricity
98      #e_dust = (1 - r/semimajor_axis)
99
100     aphelion = semimajor_axis * (1 + e_dust)  #[m]
101
102     return semimajor_axis, e_dust, aphelion
103
104
105 def get_values(beta):
106     """
107     Calculates the orbital elements for the given beta values.
108     """
109
110     semimajor_axis_circ = np.zeros(len(beta))
111     eccentricity_circ = np.zeros(len(beta))
112     aphelion_circ = np.zeros(len(beta))
113
114     for i in range(len(beta)):
115
116         a, e, rmax = orbital_elements(beta[i], velocity_parent.
            max(), r_parent[np.argmax(velocity_parent)])
117         semimajor_axis_circ[i] = abs(a)
118         eccentricity_circ[i] = abs(e)
119         aphelion_circ[i] = abs(rmax)
120
121     return semimajor_axis_circ, eccentricity_circ, aphelion_circ
122
123
124 #beta values for asteroidal grains, with values from Wilck and
        Mann (1995):
125 size_values = [0.01, 0.03, 0.10, 0.32, 1.0, 3.2, 10, 32] #
        micrometer
126 #mass_values = [4.4e-13, 1.4e-11, 4.4e-10, 1.4e-8] #g
127 beta_values = [0.106, 0.163, 0.751, 0.772, 0.222, 0.061, 0.018,
         0.005]
128
129 #interpolating the above values:
130 interpfunc = interp1d(np.log10(size_values), np.log10(
```

```
    beta_values), kind = 'quadratic')
size_asteroidal = np.geomspace(size_values[0], size_values[-1],
     200)
beta_asteroidal = 10**interpfunc(np.log10(size_asteroidal))


def open_file(filename, variable_column):
    """
    Function that reads a file and returns the wanted variable
    """
    with open(filename, 'r', newline='') as file:

        lines = file.readlines()
        del lines[0]

        variable_s = [line.split()[variable_column] for line in
    lines]
        variable = [float(num) for num in variable_s]
        print(variable)

    return np.array(variable)

#beta values from Aigen Li (personal communication):
radius_waterice = open_file('C:\\Users\\eier\\OneDrive\\
    Documents\\FYS-3931\\ice_radpr_prdrag_sun1au.dat', 0) * 1e
    -6 #m
beta_waterice = open_file('C:\\Users\\eier\\OneDrive\\Documents
    \\FYS-3931\\ice_radpr_prdrag_sun1au.dat', 1)


#beta values calculated with equation 2.4:
Q_pr = 1
rho = 2  #g cm^-3
s = radius_waterice * 1e2
#rho and s are in cgs units
#betaval = 3 * L/(16 * np.pi * G * M * c) * Q_pr/(rho * s)
beta_eq19 = 5.7e-5 * Q_pr/(rho * s)


#interpolating the radius and beta between 1 and 10 um:
radius_new_array = np.linspace(1, 10, 100)

def interpolate_beta(radius_old, beta_old):
    intp_beta = interp1d(radius_old, beta_old)
    beta_new = intp_beta(radius_new_array)
    return beta_new

beta_asteroidal_2 = interpolate_beta(size_asteroidal,
    beta_asteroidal)
beta_waterice_2 = interpolate_beta(radius_waterice*1e6,
    beta_waterice)
beta_eq19_2 = interpolate_beta(radius_waterice*1e6, beta_eq19)


```

```
177 #defining time array and solving Kepler's equation for the
        parent object:
178 t_parent = np.linspace(0, tau(semimajoraxis_parent, 0), 10000)
179 r_parent, rx_parent, ry_parent = Kepler_elliptical(t_parent,
        semimajoraxis_parent, eccentricity_parent, 0)
180 velocity_parent = velocity(semimajoraxis_parent, r_parent, 0)
181
182
183 #computing the orbital elements:
184 a_asteroidal, e_asteroidal, aph_asteroidal = get_values(
        beta_asteroidal_2)
185 a_waterice, e_waterice, aph_waterice = get_values(
        beta_waterice_2)
186 a_eq19, e_eq19, aph_eq19 = get_values(beta_eq19_2)
187
188
189 def position(semimajor_axis, eccentricity, beta_values,
        parentvel):
190     """
191     Retrieves the position of the grains.
192     """
193
194     r = []
195     time_arrays = []
196     aphelions = []
197     perihelions = []
198     orbital_periods = []
199     for i in range(len(beta_values)):
200         if 0 <= abs(eccentricity[i]) < 1:
201             t_dust = np.linspace(0, tau(semimajor_axis[i],
        beta_values[i]), 10000)
202             time_arrays.append(t_dust)
203             pos, rx, ry = Kepler_elliptical(t_dust, semimajor_axis
        [i], eccentricity[i], beta_values[i])
204             r.append((pos, rx, ry))
205             aphelions.append(pos.max())
206             perihelions.append(pos.min())
207             orbital_periods.append(tau(semimajor_axis[i],
        beta_values[i]))
208
209     rr = np.array(r)
210     return rr, time_arrays, orbit_type, np.array(perihelions),
        np.array(aphelions), np.array(orbital_periods)
211
212
213 rr_asteroidal, time_asteroidal, orbittype_asteroidal,
        velocities_asteroidal, perihelions_asteroidal,
        aphelions_asteroidal, orbitperiod_asteroidal = position(
        a_asteroidal, e_asteroidal, beta_asteroidal_2,
        velocity_parent.max())
214 rr_waterice, time_waterice, orbittype_waterice,
        velocities_waterice, perihelions_waterice,
        aphelions_waterice, orbitperiod_waterice = position(
        a_waterice, e_waterice, beta_waterice_2, velocity_parent.
```

```
    max())
rr_eq19, time_eq19, orbittype_eq19, velocities_eq19,
    perihelions_eq19, aphelions_eq19, orbitperiod_eq19 =
    position(a_eq19, e_eq19, beta_eq19_2, velocity_parent.max()
    )
```

Listing C.2: Code used to solve Kepler's equation for grains with different beta-values.

```
import os
import numpy as np
import matplotlib.pyplot as plt
import matplotlib.colors as cl

AU = 1.496e+11     #AU to meters
yrstosec = 3.154e+7      #years to seconds

def compute_heliocentric_dist(path):
    """
    Function that reads all the output files from the model.
    Calculates and returns the heliocentric distance for all
    the grains.
    """

    #reading all the files from the path:
    files = os.listdir(path)
    dat_files = [f for f in files if f.endswith('.dat')]

    #concatinating all the data from the files into a single
    array:
    data = np.concatenate([np.fromfile(os.path.join(path, f),
    dtype=np.float32) for f in dat_files])
    data = data.reshape(-1, 9)

    #defining the position vector:
    r = data[:, 2:5] * AU

    heliocentric_distance = np.linalg.norm(r, axis=1)    #[m]

    return r/AU, heliocentric_distance/AU

r_1um, heliodist_1um = read_dat_files('path')
r_10um, heliodist_10um = read_dat_files('path')
r_100um, heliodist_100um = read_dat_files('path')


def read_dat_files2(path):
    """
    Function that reads all the output files from the model, and
      iterates through each file. Calculates the eccentricity
    and semi-major axis for each grain.
    """

    #reading all the files from the path:
    files = os.listdir(path)
```

```
42    dat_files = [os.path.join(path, f) for f in files if f.
      endswith('.dat')]
43
44    #defining empty lists:
45    eccentricity_array = []
46    semimajorax_array = []
47
48    #iterating through each file:
49    for file in dat_files:
50       data = np.fromfile(os.path.join(path, file), dtype=np.
      float32)
51       data = data.reshape(-1, 9)
52
53       r = data[:, 2:5] * AU
54       v = data[:, 5:8] * AU / yrstosec
55
56       heliocentric_distance = np.linalg.norm(r, axis=1)    #[m]
57
58       def find_local_extrema_indices(arr):
59          """
60          Function that iterates through an array and finds the
      local extrema per orbit.
61          """
62
63          #empty lists for maximum and minimum values of the
      heliocentric distance per orbit:
64          local_minima = []
65          local_minima_time = []
66          local_maxima = []
67          local_maxima_time = []
68
69          for i in range(1, len(arr) - 1):
70             if arr[i] < arr[i - 1] and arr[i] < arr[i + 1]:
71                local_minima.append(arr[i])
72                local_minima_time.append(data[i, 0])
73             elif arr[i] > arr[i - 1] and arr[i] > arr[i + 1]:
74                local_maxima.append(arr[i])
75                local_maxima_time.append(data[i, 0])
76
77          return np.array(local_minima), np.array(
      local_minima_time), np.array(local_maxima), np.array(
      local_maxima_time)
78
79
80       local_minima, local_minima_time, local_maxima,
      local_maxima_time = find_local_extrema_indices(
      heliocentric_distance)
81
82
83       min_length = min(len(local_minima), len(local_maxima))
84
85       local_minima = local_minima[:min_length]
86       local_minima_time = local_minima_time[:min_length]
87       local_maxima = local_maxima[:min_length]
```

```
88        local_maxima_time = local_maxima_time[:min_length]
89
90        e2 = (local_maxima - local_minima)/(local_maxima +
      local_minima)
91        semimajor_axis = (local_maxima + local_minima)/2
92
93              eccentricity_array.append(e2)
94              semimajorax_array.append(semimajor_axis)
95
96
97     return eccentricity_array, np.array(semimajorax_array)/AU
98
99
100 e_1um, a_1um = read_dat_files2('path')
101 e_10um, a_10um = read_dat_files2('path')
102 e_100um, a_100um = read_dat_files2('path')
```

Listing C.3: Code used to read the output from the model and calculate the heliocentric distance, eccentricty and semi-major axis of the grains.